

BEoRN: A fast and flexible framework to simulate the epoch of reionisation and cosmic dawn

Timothée Schaeffer^{1*}, Sambit K. Giri^{1,2}, and Aurel Schneider¹

¹*Center for Theoretical Astrophysics and Cosmology, Institute for Computational Science, University of Zurich, Winterthurerstrasse 190, CH-8057 Zurich, Switzerland*

²*Nordita, KTH Royal Institute of Technology and Stockholm University, Hannes Alfvéns väg 12, SE-106 91 Stockholm, Sweden*

Accepted XXX. Received YYY; in original form ZZZ; Report Number NORDITA 2023-019

ABSTRACT

In this study, we introduce BEoRN (Bubbles during the Epoch of Reionisation Numerical Simulator), a publicly available Python code that generates three-dimensional maps of the 21-cm signal from the cosmic dawn and the epoch of reionisation. Built upon N -body simulation outputs, BEoRN populates haloes with stars and galaxies based on a flexible source model. It then computes the evolution of Lyman- α coupling, temperature, and ionisation profiles as a function of source properties, and paints these profiles around each source onto a three-dimensional grid. The code consistently deals with the overlap of ionised bubbles by redistributing photons around the bubble boundaries, thereby ensuring photon conservation. It accounts for the redshifting of photons and the source look-back effect for the temperature and Lyman- α coupling profiles which extend far into the intergalactic medium to scales of order 100 cMpc. We provide a detailed description of the code and compare it to results from the literature. After validation, we run three different benchmark models based on a cosmological N -body simulation. All three models agree with current observations from UV luminosity functions and estimates of the mean ionisation fraction. Due to different assumptions regarding the small-mass stellar-to-halo relation, the X-ray flux emission, and the ionising photon escape fraction, the models produce unique signatures ranging from a cold reionisation with deep absorption trough to an emission-dominated 21-cm signal, broadly encompassing the current uncertainties at cosmic dawn. The code BEoRN is publicly available at <https://github.com/cosmic-reionization/BEoRN>.

Key words: radiative transfer, galaxies: formation, intergalactic medium, cosmology: theory, dark ages, reionization, first stars, X-rays: galaxies

1 INTRODUCTION

The hyperfine transition of neutral hydrogen generates photons at the wavelength of 21 cm, opening a new observational window into the early Universe approximately one billion years after the Big Bang. During this era, the radiation from the first stars and galaxies pushes the spin temperature out of equilibrium before heating and eventually ionising the neutral hydrogen of the intergalactic medium (IGM). Next to the source properties, the 21-cm signal depends on the clustering and temperature distribution of the neutral gas, the primordial background radio emission, and the detailed interaction processes between radiation and matter. It is therefore not surprising that the 21-cm radiation from the cosmic dawn contains a wealth of information about the properties of the first stars (Fialkov & Barkana 2014; Mirocha et al. 2018; Ventura et al. 2023; Sartorio et al. 2023), galaxies (Park et al. 2019; Reis et al. 2020; Hutter et al. 2021), and black holes (Pritchard & Furlanetto 2007; Ross et al. 2019). It can furthermore be used to constrain the cosmological model (Liu & Parsons 2016; Schneider et al. 2023; Shmueli et al. 2023) and, in particular, the dark sector, such as the nature of dark matter (Sitwell et al. 2014; Chatterjee et al. 2019; Nebrin et al. 2019; Muñoz et al.

2020; Jones et al. 2021; Giri & Schneider 2022; Hotinli et al. 2022; Flitter & Kovetz 2022; Hibbard et al. 2022), interactions between the dark and visible sector (Barkana et al. 2018; Fialkov et al. 2018; Kovetz et al. 2018; Lopez-Honorez et al. 2019; Mosbech et al. 2023), or potential exotic decay and annihilation processes (D’Amico et al. 2018; Liu & Slatyer 2018; Mitridate & Podo 2018).

Reliable detection of the 21-cm signal at these redshifts has yet to be achieved, but ongoing experiments, such as the Giant Metrewave Radio Telescope (GMRT, Paciga et al. 2013), the Precision Array for Probing the Epoch of Reionization (PAPER, Kolopanis et al. 2019), the Murchison Widefield Array (MWA, Trott et al. 2020), the Low-Frequency ARray (LOFAR, Mertens et al. 2020), and the Hydrogen Epoch of Reionization Array (HERA, The HERA Collaboration et al. 2023) have provided upper limits on the 21-cm power spectrum for a broad range of redshifts. These bounds have been used to exclude regions of the parameter space describing extreme properties of the IGM during the epoch of reionisation (Ghara et al. 2020, 2021; Greig et al. 2021a,b; The HERA Collaboration et al. 2022a).

The Square Kilometre Array (SKA), a next-generation radio interferometer, is currently under construction in South Africa and Western Australia. Its low-frequency component, SKA-low, has the capability to not only measure the 21-cm power spectrum with high signal-to-noise ratio but also provide sky images at redshifts around

* E-mail: timothee.schaeffer@uzh.ch

$z \approx 5 - 25$ (e.g. Mellema et al. 2015; Wyithe et al. 2015; Ghara et al. 2017; Giri et al. 2018a; Bianco et al. 2021b). The potential of SKA-low for studying the cosmic dawn and reionization era has been extensively investigated in various studies, exploring properties of the ionizing sources and the ionization structure of the universe (e.g. Giri et al. 2018b; Zackrisson et al. 2020; Giri & Mellema 2021; Gazagnes et al. 2021; Bianco et al. 2023). These studies highlight the significant role that SKA-low will play in advancing our understanding of these critical cosmic epochs.

Next to the tremendous experimental effort, accurate and reliable theoretical methods to model the 21-cm signal at the required accuracy level are currently being developed. Modelling the 21-cm signal is challenging as it involves a broad dynamical range from minihaloes to cosmological scales. It depends on the details of hydrodynamical feedback processes for galaxies, the propagation of radiation through large cosmological scales, and the detailed interaction processes of photons with gas particles of the IGM (e.g., Iliiev et al. 2006; Mellema et al. 2006b; Trac & Cen 2007).

One option is to predict the 21-cm signal with the help of coupled radiative-transfer hydrodynamic simulations, some well-known examples being the Cosmic Dawn (CoDA) (Ocvirk et al. 2016; Ocvirk et al. 2020; Lewis et al. 2022), the 21SSD (Semelin et al. 2017), and the THESAN simulations (Kannan et al. 2022; Garaldi et al. 2022). Another option is to post-process N-body simulations with ray-tracing algorithms, such as the Conservative, Causal Ray-tracing code (C²RAY; Mellema et al. 2006a) or the Cosmological Radiative transfer Scheme for Hydrodynamics (CRASH; Maselli et al. 2003). Full radiative-transfer numerical methods are fundamental to understanding the 21-cm signal and estimating the accuracy of more approximate methods. However, they are very computationally expensive and can hardly be used to scan the vast cosmological and astrophysical parameter space. To perform Bayesian inference analysis on a mock 21-cm data set, semi-numerical algorithms are often used, better suited to generate thousands of realizations of the signal itself. They rely on the excursion set formalism (Furlanetto et al. 2004), such as 21cmFAST (Mesinger et al. 2011) or SIMFAST21 (Santos et al. 2010).

In this paper, we present the new framework BEoRN which stands for *Bubbles during the Epoch of Reionisation Numerical simulator*. The code is based on a one-dimensional radiative transfer method in which interactions between matter and radiation are treated in a spherically symmetric way around sources. This approach is significantly faster than full 3-d radiative transfer codes and arguably more precise than semi-numerical algorithms which are not based on individual sources. In this aspect, BEoRN is similar to other existing codes such as BEARS (Thomas et al. 2009) or GRIZZLY (Ghara et al. 2018). However, in contrast to other 1d radiative transfer codes, BEoRN self-consistently accounts for the evolution of individual sources during the emission of photons. This includes both the redshifting of photons due to the expansion of space and the increase of luminosity caused by the growth of individual sources over time. Both effects have a non-negligible influence on the radiation profile surrounding sources.

The BEoRN framework allows for a flexible parametrisation to model any source of radiation, such as e.g. Pop-III stars, galaxies, or quasars. It produces a 3-dimensional (3D) light-cone realisation of the 21-cm signal from the cosmic dawn to the end of reionisation including redshift space distortion effects. The underlying gas density field as well as the position of sources is directly obtained from outputs of an N -body simulation. We have designed BEoRN to be user-friendly and modular so that it can be applied in combination with different gravity solvers or source models, for example.

The paper is structured as follows: Section 2 describes the BEoRN code, while section 3 validates it by comparing its predictions with the publicly available 21cmFAST code. In section 4, three benchmark models are presented, calibrated to the latest observations, and the evolution of the 21-cm signal during the cosmic dawn and epoch of reionization is studied. The work concludes with a summary and conclusion in section 5.

Note that throughout the paper, physical distance units are specified with the prefix "p", while co-moving distance units are specified with the prefix "c". The cosmological parameters used in this work are consistent with Planck 2018 results (Planck Collaboration et al. 2020), namely matter abundance $\Omega_m = 0.31$, baryon abundance $\Omega_b = 0.045$, and dimensionless Hubble constant $h = 0.68$. The standard deviation of matter perturbations at $8h^{-1}$ cMpc scale is $\sigma_8 = 0.81$.

2 MODELLING THE 21-CM SIGNAL

2.1 21-cm differential brightness temperature

Radio interferometers measure the 21-cm signal against the Cosmic Microwave Background (CMB) radiation. This so-called differential brightness temperature (dT_b) is a function of position (\mathbf{x}) and redshift (z) given by (e.g. Furlanetto et al. 2006)

$$dT_b(\mathbf{x}, z) = 27(1 - x_{\text{HII}}(\mathbf{x}, z))(1 + \delta_b(\mathbf{x}, z)) \left(\frac{0.15}{\Omega_m h^2} \frac{(1+z)}{10} \right)^{\frac{1}{2}} \times \left(\frac{\Omega_b h^2}{0.023} \right) \frac{x_{\text{tot}}(\mathbf{x}, z)}{1 + x_{\text{tot}}(\mathbf{x}, z)} \left(1 - \frac{T_\gamma(z)}{T_k(\mathbf{x}, z)} \right) \text{ [mK]}, \quad (1)$$

where T_γ is the cosmic microwave background (CMB) temperature, T_k is the kinetic temperature of the gas, x_{HII} is the local fraction of ionised hydrogen, and δ_b the baryon overdensity. The total coupling coefficient is defined as the sum of the collisional and Lyman- α coupling coefficients, i.e., $x_{\text{tot}} = x_c + x_\alpha$. We compute them using the following expressions:

$$x_\alpha(\mathbf{x}, z) = \frac{1.81 \times 10^{11}}{(1+z)} S_\alpha J_\alpha(\mathbf{x}, z), \quad (2)$$

and

$$x_c(\mathbf{x}, z) = \frac{T_*}{A_{10} T_\gamma(z)} \sum_i n_i(z) \kappa_{10}^i(T_k), \quad (3)$$

where S_α is given by Eq. (55) in Furlanetto et al. (2006) and $J_\alpha(\mathbf{x}, z)$ is the local flux of Lyman- α photons in [$\text{pcm}^{-2} \text{sr}^{-1} \text{Hz}^{-1} \text{s}^{-1}$]. κ_{10}^i [$\text{cm}^3 \text{s}^{-1}$] is the rate coefficient for spin de-excitation in collisions with species i , and depends on the local temperature of the gas, and hence, on the position (\mathbf{x}). The sum is done over $i = \{e^-, H\}$, i.e. hydrogen atoms and free electrons, with densities n_i [cm^{-3}]. A_{10} [s^{-1}] is the Einstein coefficient for spontaneous emission, and $T_* = 68$ mK the temperature associated with the hyperfine transition.

The peculiar velocity of the gas in the IGM will modulate the observed frequency of the 21-cm signal (see e.g. eq. 6 in Ross et al. 2021). This phenomenon, known as redshift space distortion (RSD Kaiser 1987), will significantly impact the signal, see e.g. Mao et al. (2012); Jensen et al. (2013) and Ross et al. (2021) for a detailed study on this. The observed data by radio interferometers will contain the 21-cm signal spatially distributed in the sky and evolving along with observed frequency or redshift. This 3D data is known as the lightcone. We account for RSD using the scheme described in Jensen et al. (2013) and create the 21-cm signal lightcone using the method in Datta et al. (2012), which are implemented in the publicly available package TOOLS21CM (Giri et al. 2020).

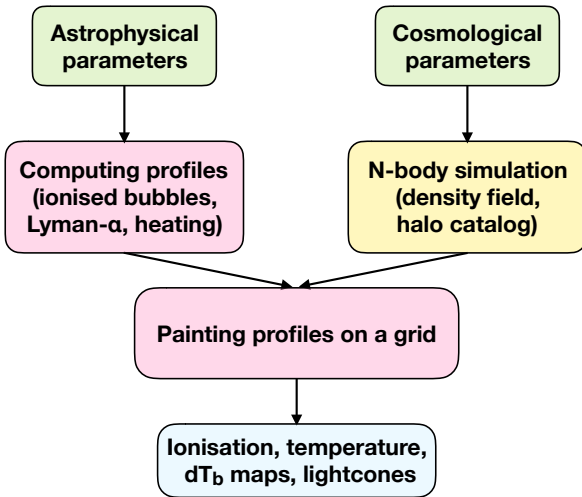


Figure 1. General structure of the BEoRN code. On the one hand, the astrophysical source parameters determine the size of ionised bubbles, the gas temperature profiles and the Lyman- α flux profiles. On the other hand, the cosmological parameters control the properties of the matter density field and the abundance of DM haloes, obtained from N-body simulations. The profiles are painted on a 3D grid, centred on DM haloes. The end-product of the code are ionisation, kinetic temperature and 21-cm brightness temperature maps including redshift space distortions, as well as lightcones.

2.2 Methodology of BEoRN

The objective of BEoRN is to produce brightness temperature (dT_b) maps on 3D grids, from the beginning of cosmic dawn to the end of the reionisation process. We thereby assume spherical symmetry around sources regarding the photon emission, the gas heating and the Lyman- α coupling processes. In this way we can describe the propagation of photons and the radiation-matter interactions with a set of one-dimensional profiles, greatly simplifying our analysis. Different profiles may overlap leading to complex, non-symmetrical patterns around sources.

While the temperature and Lyman- α coupling are additive in the sense that profiles from different sources acting on one gas volume can simply be summed up, this is not the case for the ionisation process. In this case, overlapping profiles have to be corrected by redistributing excess photons in order to guarantee photon number conservation. Note that such an approach has been shown to provide accurate patterns of ionisation (Ghara et al. 2018).

We summarise the basic algorithm of BEoRN in the following steps:

(i) Assuming an astrophysical source model, BEoRN first computes the evolution of 1D ionisation, Lyman- α and temperature profiles for a discrete set of halo masses (between $M \approx 10^5$ and $10^{15} M_\odot$). It thereby assumes haloes to grow according to a universal Mass Accretion Rate (MAR) model from the cosmic dawn ($z > 30$) to the end of reionisation ($z < 6$).

(ii) As a next step, these pre-computed spherical profiles are painted onto a 3d grid. They are centred around sources which are assumed to inhabit haloes obtained from a pre-run N-body simulation. Regarding the gas density field, BEoRN does not assume profiles but directly uses the outputs from the N-body simulations.

(iii) In order to account for the overlap of ionised bubbles, the “overionised” cells are redistributed to the bubble outskirts, ensuring photon conservation.

(iv) The resulting dT_b signal is obtained by combining the temperature (T_k), ionisation (x_{HII}), and Lyman- α coupling (x_α) maps for each redshift according to Eq. (1). Finally, all outputs are corrected for the RSD effect and combined to obtain a light cone prediction of the 21-cm signal.

In the next sections, we present the different ingredients of the framework in more detail. In particular we discuss the underlying N-body simulations (Sec. 2.3), the implementation of the source model (Sec. 2.4), the calculation of the source profiles (Sec. 2.5), the painting algorithm (Sec. 2.6), and the redistribution of ionising photons to ensure photon conservation (Sec. 2.6.2).

2.3 Density field and dark matter haloes

As initial input, the BEoRN framework requires a 3D density field and a corresponding halo catalogue (with positions) for different redshifts. We use outputs from N-body simulations run with Pkdgrav3 (Potter et al. 2017) but other methods are applicable as well. For example, a significant speed-up of the code could be achieved by using density fields from Lagrangian perturbation theory combined with halo catalogues from excursion set modelling. Another option would be to couple BEoRN with fast and approximate gravity codes such as COLA (COmoving Lagrangian Acceleration; Tassev et al. 2015) or FAST-PM (Feng et al. 2016).

Our algorithm assumes that sources reside at the center of dark matter haloes and that baryonic gas tracks dark matter such that their overdensities are identical ($\delta_b = \delta_m$). These assumptions are expected to be valid for the scales of interest, especially for the most relevant wave modes $0.1 \lesssim k \lesssim 3 \text{ Mpc}^{-1}$.

2.4 Source modelling

In this section, we present the source parameterisation used in BEoRN which is motivated by the model presented in Schneider et al. (2021, 2023). In general, any emitted radiation is connected to the mass of the source halo (M_h) as well as its accretion rate (\dot{M}_h). We will first define the star-formation rate before providing details about the spectral distribution of photons. For the latter, we assume independent parameterisations for the three spectral bands of the X-ray regime, the UV regime beyond the Lyman-limit frequency, and the UV regime between the Lyman- α and Lyman-limit frequencies.

2.4.1 Star formation rate

We relate the star formation rate (SFR) of sources with the halo accretion rate via the relation

$$\dot{M}_* = f_*(M_h) \dot{M}_h, \quad (4)$$

where the star-formation efficiency (SFE) function is given by the double power-law

$$f_*(M_h) = \frac{2(\Omega_b/\Omega_m)f_{*,0}}{(M_h/M_p)^{\gamma_1} + (M_h/M_p)^{\gamma_2}} \times S(M_h), \quad (5)$$

with the additional low-mass term

$$S(M_h) = [1 + (M_t/M_h)^{\gamma_3}]^{\gamma_4}. \quad (6)$$

The shape of f_* is motivated by abundance matching results between observed galaxy luminosity and simulated halo mass functions at $z \approx 0 - 10$ (Behroozi et al. 2013). The term $S(M_h)$ may either act as a truncation or an enhancement term of the SFE at small halo masses (depending on the parameter choices of γ_3 and γ_4) accounting for

our current ignorance of the star formation process at the smallest scales.

At high redshifts, the mass growth of haloes is known to be well described by an exponential function of the form

$$M_h(z) = M_h(z_0) \exp[-\alpha(z - z_0)], \quad (7)$$

with $\alpha = 0.79$ (Dekel et al. 2013). We use this exponential model (EXP) in this paper. In the left-most panel of Fig. 2, we illustrate the agreement of the exponential halo growth model (black line) with simulations from (Behroozi et al. 2020). Other methods exist to quantify the growth of haloes, relying on Abundance Matching or on the extended Press-Schechter formalism (Schneider et al. 2021). They are also implemented in BEoRN.

2.4.2 Lyman- α emissivity

The emissivity ϵ_α [$\text{s}^{-1}\text{Hz}^{-1}(M_\odot/\text{yr})^{-1}$] of UV photons between the Lyman- α (ν_α) and Lyman-limit (ν_{LL}) frequencies is given by

$$\epsilon_\alpha(\nu) = \frac{N_\alpha}{m_p} I_\alpha(\nu), \quad (8)$$

where $I_\alpha(\nu) \propto \nu^{-\alpha_s}$ in [Hz^{-1}] is the normalised spectral shape function, m_p is the proton mass (expressed in M_\odot), and N_α the number of photons per baryons in stars emitted between ν_α and ν_{LL} . Typical values are $N_\alpha = 9690, 4800$, respectively for Population II, and Population III stars (Barkana & Loeb 2005).

2.4.3 X-ray emissivity

The emissivity ϵ_X [$\text{s}^{-1}\text{Hz}^{-1}(M_\odot/\text{yr})^{-1}$] of X-ray photons is given by

$$\epsilon_X(\nu) = c_X \cdot f_X \frac{I_X(\nu)}{\nu \cdot h_p} \quad (9)$$

where the spectrum is again assumed to have a power-law shape $I_X(\nu) \propto \nu^{-\alpha_X}$ [Hz^{-1}]. The additional normalisation factor c_X is obtained from observation by integrating X-ray fluxes of local sources (Mineo et al. 2012; Fragos et al. 2013; Mashian et al. 2015) in the energy range ($E_{\text{min,norm}}, E_{\text{max,norm}}$). The values of c_X , $E_{\text{min,norm}}$, and $E_{\text{max,norm}}$ are left free, and depend on the X-ray sources, which are usually assumed to be either high-mass X-ray binaries (HMXB) or quasars (QSO). A standard value used in the literature is $c_X = 10^{40.5}$ $\text{erg s}^{-1}\text{yr } M_\odot^{-1}$ in the energy range $E_{\text{min,norm}} = 500$ eV, $E_{\text{max,norm}} = 2$ keV (Park et al. 2019), but c_X remains largely unknown for high redshift sources. Lastly, to account for the absorption of soft X-ray photons by the host galaxy (Das et al. 2017), we only allow the X-ray spectrum to extend over an energy range [$E_{\text{min}}, E_{\text{max}}$]. Reducing the value of E_{min} can significantly increase the heating of the gas by allowing for more soft X-ray photons to reach the IGM.

2.4.4 Ionising photons

We parametrise the galactic ionising radiation differently than the Lyman- α and X-ray components. Instead of a frequency-dependent spectrum, we only account for the total number of photons with energy larger than 13.6 eV emitted per unit time (\dot{N}_{ion}):

$$\dot{N}_{\text{ion}}(M_h) = f_{\text{esc}}(M_h) f_*(M_h) \dot{M}_h \times \frac{N_{\text{ion}}}{m_p}, \quad (10)$$

where N_{ion} stands for the number of ionising photons per baryons in stars, and f_{esc} is the escape fraction of ionising photons. The escape

fraction is assumed to scale as a power law

$$f_{\text{esc}}(M_h) = f_{\text{esc},10}(M_h) \left(\frac{10^{10} M_\odot}{M_h} \right)^{\alpha_{\text{esc}}}. \quad (11)$$

The function is truncated so that $f_{\text{esc}} \leq 1$. Note that radiative-hydrodynamical simulations point towards a decreasing f_{esc} with halo mass, which is explained by the low column density of gas in small mass galaxies (Paardekooper et al. 2015; Kimm et al. 2017; Lewis et al. 2020).

Note that to calculate the emission rate of photons in the Lyman- α and X-ray bands (Eq. 8 and 9, respectively), the SFR obtained from the halo mass via Eq. 4 and 7 needs to be multiplied. On the other hand, the ionizing photon rate is directly provided by Eq. 10.

2.5 Radial profiles

As mentioned in the beginning, one of the core ingredients of the BEoRN framework are the spherically symmetric profiles describing the Lyman- α coupling (x_α), the gas temperature (T_k), and ionization process (x_{HII}) around sources. In this section, we provide an overview of the equations governing the evolution of these profiles. More detailed descriptions of the calculations can be found in Schneider et al. (2021, 2023).

2.5.1 Lyman- α flux profiles

The interactions of the Lyman- α photons with the neutral hydrogen atoms of the IGM leads to a coupling of the spin temperature to the kinetic temperature of the gas (Wouthuysen 1952; Field 1958). This coupling causes an absorption trough in the global signal prior to the epoch of reionization. The value of the flux at a physical distance r from a source with mass M_h at time z is computed by tracing back the photons emitted at $r = 0$ at an earlier time z' , when the source had a smaller mass $M_h(z')$. This resulting flux profile is given by

$$\rho_\alpha(r|M_h, z) = \frac{1}{4\pi r^2} \sum_{n=2}^{n_m} f_n \epsilon_\alpha(\nu'_n) f_*(M_h(z')) \dot{M}_h(z') \quad (12)$$

with $\nu'_n = \nu_n(1+z')/(1+z)$, where ν_n is the frequency of the Ly α resonance, and where f_n are the recycling fractions assuming the truncation $n_m = 23$ (Pritchard & Furlanetto 2006). The look-back redshift z' is obtained by numerically inverting the comoving distance relation

$$r = \frac{1}{1+z} \int_z^{z'} \frac{c}{H(z'')} dz'', \quad (13)$$

where $H(z)$ refers to the Hubble parameter.

In the second panel of Fig. 2 we show examples of Lyman- α flux profiles for different halo masses and redshifts (as indicated by the coloured stars in the left-most panel). The underlying source model assumes a flat $f_* = 0.1$, leading to an exponential growth in the SFR. The profiles decrease as $1/r^2$ close to the source steepening gradually towards larger radii due to the look-back effect and the lower star formation rate in the past. The steep cutoff at a few hundred Mpc is due to the horizon beyond which the source becomes invisible.

2.5.2 Temperature profiles

The heating of the IGM around sources is caused by X-ray radiation which interacts with the surrounding gas cells. The relevant X-ray

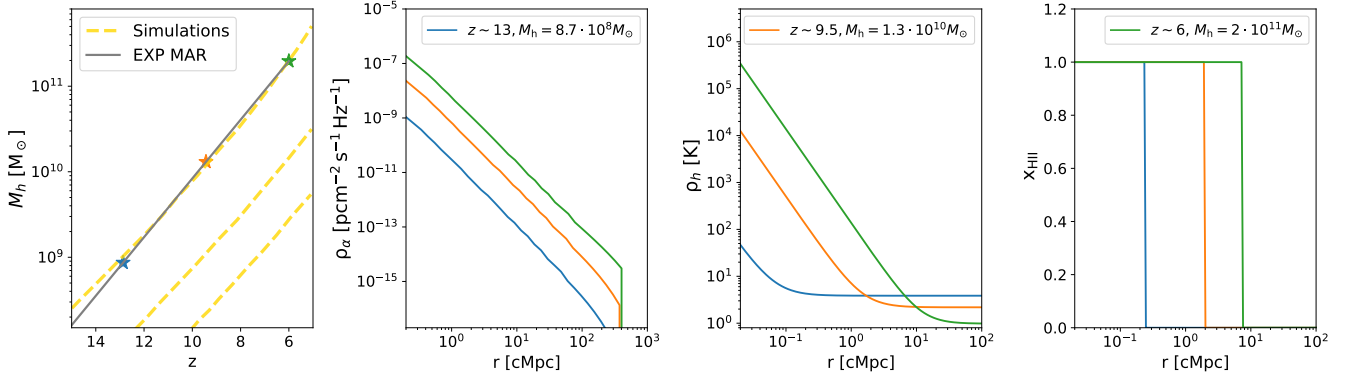


Figure 2. Halo mass growth and profiles for different masses and redshifts. *First panel:* The grey curve depicts the halo mass accretion history as predicted by the EXP MAR model (Eq. 7). We compare it to the yellow curves, obtained from simulation (Behroozi et al. 2020). *Second panel:* Profiles for the Lyman- α coupling coefficient ρ_α (Eq. 2 and 12), as a function of comoving distance r . *Third panel:* Kinetic temperature profiles T_k (Eq. 15). *Fourth panel:* Ionisation fraction profile x_{HII} (Eq. 16).

emission profiles are given by

$$\rho_{\text{xray}}(r|M, z) = \frac{1}{4\pi r^2} \sum_i f_i f_{X,h} \times \int_{\nu_{\text{th}}^i}^{\infty} d\nu (\nu - \nu_{\text{th}}^i) h_P \sigma_i(\nu) \varepsilon_X(\nu') e^{\tau_{\nu'}} f_* \dot{M}_h(z'). \quad (14)$$

where $i = \{\text{H}, \text{He}\}$ and $\nu_{\text{th}}^i = \{13.6, 26.5\}$ eV. ρ_{xray} has units of $[\text{eV}/\text{s}]$. Note that r here again is a physical distance. The mean optical depth of the IGM ($\tau_{\nu'}$) is computed according to Eq. (26) of Schneider et al. (2021). h_P is the Planck constant. $f_{X,h}$ is the amount of heat deposited by secondary electrons. We assume $f_{X,h} = \bar{x}_e^{0.225}$ (Shull & van Steenberg 1985), where \bar{x}_e is the mean free electron fraction in the neutral medium. We compute \bar{x}_e according to eq. 9, 10 and 12 in Mirocha (2014).

The temperature profile ρ_h (in [K]) of the neutral medium around a source is then obtained by solving the following differential equation:

$$\frac{3}{2} \frac{d\rho_h(r|M_h, z)}{dz} = \frac{3\rho_h(r|M_h, z)}{(1+z)} - \frac{\rho_{\text{xray}}(r|M_h, z)}{k_B(1+z)H(z)}. \quad (15)$$

We show example ρ_h profiles in the third panel of Fig. 2 that are obtained by solving Eq. 15 assuming constant adiabatic initial conditions. These profiles decrease as $1/r^2$ and reach the adiabatic cooling plateau at large radii, representing regions far away from the source where baryons have not been heated by X-ray photons yet.

2.5.3 Ionisation fraction profiles

The co-moving volume V of an HII region around a source emitting ionising photons at a rate $\dot{N}_{\text{ion}}(t)$ [s^{-1}] evolves according to:

$$\frac{dV}{dt} = \frac{\dot{N}_{\text{ion}}(t)}{\bar{n}_H^0} - \alpha_B \frac{C}{a^3} \bar{n}_H^0 V, \quad (16)$$

with α_B the case-B recombination coefficient, C the clumping factor, a the scale factor, \bar{n}_H^0 the mean co-moving number density of hydrogen. The ionisation fraction profile x_{HII} is then given by a Heaviside step function:

$$x_{\text{HII}}(r|M, z) = \theta_H [R_b(M, z) - r], \quad (17)$$

with the co-moving bubble size R_b obtained from the volume V via $V = 4\pi R_b^3/3$. Ionisation profiles are plotted in the rightmost panel of

Fig. 2. The sharp ionisation front of the bubble expands as the source grows and emits photons. Note that in our framework the clumpiness of the IGM is controlled by the parameter C . In this work, we will assume $C = 1$ for simplicity.

2.6 Constructing three dimensional maps

The aim of BEoRN is to generate 3D simulation volumes of the IGM during the epoch of reionisation and cosmic dawn, which can be observed with the 21-cm signal. To create 3D maps of the 21-cm signal or $dT_b(z, \vec{x})$, temperature, Lyman- α profiles, and ionised bubbles are painted on a grid around photon sources. To paint profiles on a grid \mathcal{G} , 3D convolution is used, which can be defined as follows:

$$\mathcal{G}(\vec{x}) = \sum_{\vec{x}_h} \int \delta_{\vec{x}_h}^{3D}(\vec{x}) \mathcal{P}(\vec{y} - \vec{x}) d\vec{x}, \quad (18)$$

where δ^{3D} is the 3D Kronecker delta function that equals one at the location of halo \vec{x}_h and zero everywhere else. As the sources are assumed to be present in dark matter haloes in a spherically symmetric environment, \mathcal{P} represents 3D grids created from the radial profiles (see Sec. 2.5).

We use an optimised version of the fast Fourier transform (FFT) based 3D convolution implemented in the `astropy`¹ package. However, the computational cost of performing this step for every halo found in the simulation becomes prohibitively high. For example, simulation volumes at redshift $z = 6$ with a box length ≥ 100 cMpc have more than 10 million haloes if we resolve halo-masses down to $\sim 10^9 M_\odot$ ². To reduce computing time, we bin halo masses and assume that every halo in a given mass bin shares the same profiles.

Let us assume we want to create dT_b coeval boxes for a range of redshifts (z_j). We first initialise an array of halo masses M_{bin} , of size N_{bin} , spanning from M_{min} to M_{max} (assuming logarithmically spaced binning), corresponding to halo masses at the final redshift z_{N_z} of the simulation. Then, we compute the mass accretion history of each mass element, backwards in time, according to the chosen MAR model (Eq. 7). We end up with a 2D array of masses ($M_{i,j}$)

¹ <https://docs.astropy.org>

² Note that the number of haloes increases both with decreasing redshift and with the resolution limit of the simulation.

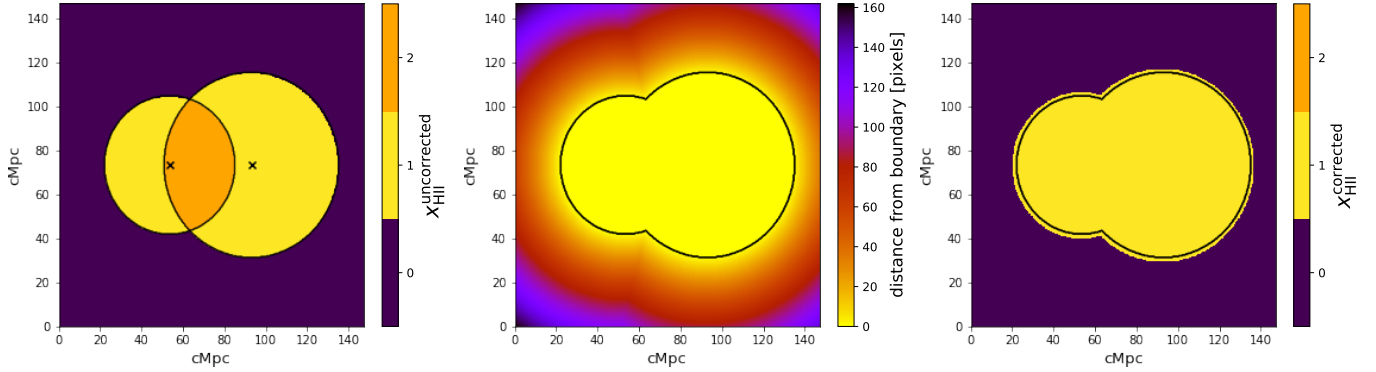


Figure 3. A toy example to illustrate how we correct for the overlap of ionised bubbles. *Left:* Two overlapping ionised bubbles before correcting for overlap. The black crosses indicate the positions of the two sources. Black contours correspond to the external border of the two ionised bubbles. The purple background corresponds to neutral hydrogen ($x_{\text{HII}} = 0$) and the yellow and orange regions to ionised pixels ($x_{\text{HII}} \geq 1$). The bubbles overlap and lead to “overionised” (orange) pixels, marked with $x_{\text{HII}} = 2$. *Middle:* We flag the background neutral pixels with their distance from the boundary of the ionised region. *Right:* The two ionised bubbles, after correcting for overlap. We have redistributed the excess ionisation fraction to a set of pixels closest to the boundary of the ionised region, which grows subsequently. We plot the same black contour as in the left panel.

with $i = 0..N_{\text{bin}}$, and $j = 0..N_z$. Finally, we compute three profiles, denoted as \mathcal{P} , for each mass bin. These profiles are obtained by evaluating Eqs. 12, 15 and 17, starting from z_0 down to z_{N_z} , while tracking the evolution of the SFR using Eq. 4. As a result, we obtain $3 \times N_z$ profiles per mass bin, leading to a total of $3 \times N_{\text{bin}} \times N_z$ profiles.

We can visualise this process through Fig. 2. The grey line in the leftmost panel shows the mass evolution of one halo mass bin, while the other panel shows the subsequent evolution of the profiles. To construct a map at a given redshift, we loop over the N_{bin} mass bins and simultaneously paint all profiles in this halo mass range. The timing of this step scales with N_{bin} . The input parameter N_{bin} , M_{min} , and M_{max} are left to the user and should be chosen such that the array of binned masses covers all halo masses included in the input halo catalogue at each redshift z_j .

We note that our approach makes two approximations: (1) we treat haloes within the same mass bin as identical, even though they have slightly different masses and hence different profiles, and (2) we assume that haloes reside at the centre of the grid cell in which their true centre is. These approximations disappear in the limit of infinite grid cells and halo mass bins. To determine a suitable number of mass bins for converged power spectra, we perform convergence checks. In Appendix B, we compare the 21-cm power spectra obtained when varying the number of grid cells N_{cell} and mass bins N_{bin} .

2.6.1 Overlap of Lyman- α and temperature profiles

Both the Lyman- α and temperature profiles typically extend far beyond the corresponding halo boundaries. As a consequence, many regions of the IGM will be inside the area of influence of two or several profiles from different neighbouring sources. For the case of the Lyman- α and X-ray emission, it is obvious that multiple contributions from different sources can be added up to obtain a total flux per gas cell.

Regarding the heating of the gas, the situation is more complicated as the temperature is obtained via a differential equation (Eq. 15). Following Schneider et al. (2021), we separate the temperature field $T_{\text{k}}(x, z)$ into a heating term $T_{\text{h}}(x, z)$, and a primordial component

$T_{\text{p}}(x, z)$, such that $T_{\text{k}} = T_{\text{p}} + T_{\text{h}}$. The primordial component is sourced by the matter fluctuations and evolves according to

$$T_{\text{p}}(x, z) = T_{\text{ad}}(z)(1 + \delta_b(x))^{2/3}, \quad (19)$$

where $T_{\text{ad}} \propto (1 + z)^2$ corresponds to the adiabatic gas temperature that decoupled from the CMB temperature at $z \sim 135$.

The heating term T_{h} is obtained by summing up all radial profile components ρ_{heat} that affect the IGM at a given position. This summation procedure becomes possible uniquely due to the simple form of Eq. 15. If we consider, for example, two separate sources with X-ray flux profiles ($\rho_{\text{xray},1}, \rho_{\text{xray},2}$), leading to temperature profiles ($\rho_{\text{h},1}, \rho_{\text{h},2}$), the solution of Eq. 15 for a source with x-ray profile $\rho_{\text{xray},1} + \rho_{\text{xray},2}$ is $\rho_{\text{h},1} + \rho_{\text{h},2}$. Hence, we are allowed to add up on a grid the heating profiles ρ_{h} from different sources. The final gas temperature maps $T_{\text{k}}(x, z)$ are obtained by adding T_{p} and T_{h} .

Note that the additive nature of temperature is tied to the simplicity, separability, and linearity of Eq. 15, a differential equation. However, this characteristic is lost when considering a spatially varying x_e component, which, in principle, influences the temperature calculation (see e.g., eq. 11 of Mesinger et al. 2011). Nevertheless, we have verified that the additional term associated with x_e remains negligible for all individual profiles. Hence, it can be safely disregarded.

2.6.2 Overlap of ionisation bubbles

In contrast to the Lyman- α and temperature profiles, the ionising bubbles are not additive. Any gas cell can only be ionised once. This means that x_{HII} has to stay between 0 and 1.

The painting process described by Eq. 18 will naturally add up profiles giving rise to pixels with $x_{\text{HII}} > 1$. In order to guarantee photon conservation, we have to take care of these “overionised” cells and distribute the excess ionisation fraction in a consistent way. Fig. 3 shows our approach for handling the overlap of ionised bubbles. In the illustrated example, we consider a system with two distinct sources that produce two overlapping bubbles. The left panel shows the resulting system after we paint the bubbles on a grid but before correcting for the overlap. The orange region indicates where the bubbles overlap and is marked with an unphysical ionising

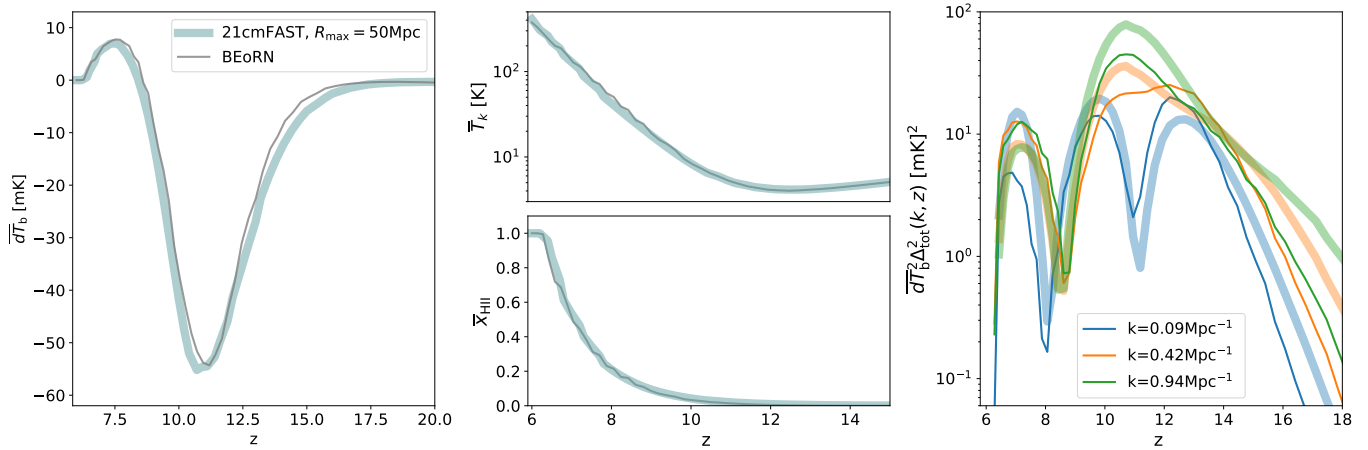


Figure 4. Comparison between 21cmFAST (thick lines in the four panels) and BEoRN (thin lines). RSD are not included. *Left:* Global differential brightness temperature dT_b . *Upper middle:* Mean kinetic temperature of the gas T_k . *Lower middle:* Mean ionisation fraction history x_{HII} . *Right:* Dimensionless power spectrum of the dT_b field, shown as a function of redshift z , at three different scales, $k = 0.09, 0.42, 0.94 \text{ Mpc}^{-1}$ respectively in blue, orange and green.

fraction of $x_{\text{HII}} = 2$. We note that this problem is similar in nature to the photon non-conservation issue discussed in e.g. Choudhury & Paranjape (2018).

Realistic simulations will contain a large number of overlapping regions. We identify all these regions using the method implemented in `skimage`³ package to label connected components (Fiorio & Gustedt 1996; Wu et al. 2005). If these connected regions contain "overionised" cells, we use the distance transform algorithm in the `scipy`⁴ package that gives the distance from the nearest boundary in terms of number of pixels. As we need to distribute the excess ionisation in the neutral pixels, we run this algorithm to get distance $d = 0$ inside ionised regions and $d > 0$ outside. This process is illustrated in the middle panel of Fig. 3. We distribute the excess ionisation among the neutral pixels by weighting over the distances. The excess ionisation is distributed only after pixels at a shorter distance have been fully ionised. In the right panel of Fig. 3, we show the system after redistributing the excess ionisation fraction to the border of the ionised region. As a result, the overall ionised island expanded proportionately to the volume of the overlapping region.

At early epochs of reionisation, the procedure of redistributing photons is time-consuming as there is a plethora of very small ionised regions that only contain a few ionised pixels. In order to speed up the code, we introduce a parameter $N_{\text{cell,th}}$, which groups all small ionised islands containing fewer than $N_{\text{cell,th}}$ pixels together. In Appendix A we show the effects of increasing $N_{\text{cell,th}}$ on the x_{HII} power spectrum. By choosing an appropriate value for $N_{\text{cell,th}}$, we can significantly reduce the computing time of the code without affecting the power spectrum over the scales relevant for 21-cm interferometers. Unless stated otherwise, we use the default value $N_{\text{cell,th}} = 160 \times (N_{\text{cell}}/256^3)$, with N_{cell} the total number of pixels.

3 VALIDATION OF OUR FRAMEWORK

As a next step, we validate BEoRN by comparing it to the widely used semi-numerical simulation code 21cmFAST⁵ (Mesinger et al. 2011). In 21cmFAST, the matter density field is evolved perturbatively according to the Zel'Dovich approximation. Ionisation maps are created based on the excursion set formalism (Furlanetto et al. 2004). This approach is fundamentally different from BEoRN since sources are not resolved individually. Instead, ionisation, Lyman- α coupling, and heating rates are computed from the collapsed fraction field f_{coll} , obtained by integrating the Press-Schechter sub-halo mass function. Furthermore, in 21cmFAST the stellar-to-halo relation and the star formation rate are computed differently than in BEoRN (see eq. 2-3 in Park et al. 2019), the spectral energy distribution of Lyman- α photons is obtained assuming the piece-wise power-law interpolation from Barkana & Loeb (2005), and inhomogeneous recombinations are implemented. It is therefore difficult to find an exact mapping between the 21cmFAST and BEoRN source parameters, and a certain amount of recalibration is required for a comparison.

The comparison is performed by (i) running 21cmFAST for a generic set of astrophysical and cosmological parameters, (ii) extracting the halo catalogues and density field produced by 21cmFAST as input files for BEoRN, (iii) re-calibrating, if needed, the intensity of Lyman- α , X-ray, and ionising radiation of BEoRN (controlled by N_α , f_X , and N_{ion}), in order to match the relevant global quantities between the two codes (i.e the temperature T_k , the ionisation history x_{HII} , and the 21-cm global signal dT_b). Once the global quantities agree, we compare the power spectra of the dT_b fields at different redshifts and k -modes. The re-calibration of the global parameters is discussed in Sec. 3.1.

We run 21cmFAST assuming a coarse and fine grid resolution (DIM, HII_DIM) of 300^3 and 900^3 cells, in a box with side length equal to 147 cMpc. The parameter controlling the maximum size of

⁵ This code is under constant development and therefore multiple versions are available. In this work, we used the C version that can be found at <https://github.com/andreimesinger/21cmFAST>. The python-wrapped version of 21cmFAST (Murray et al. 2020) is currently being upgraded with more accurate gravity evolution calculation (Andrei Mesinger, private communication) and we plan to provide an interface in BEoRN to this version.

³ <https://scikit-image.org/>

⁴ <https://scipy.org/>

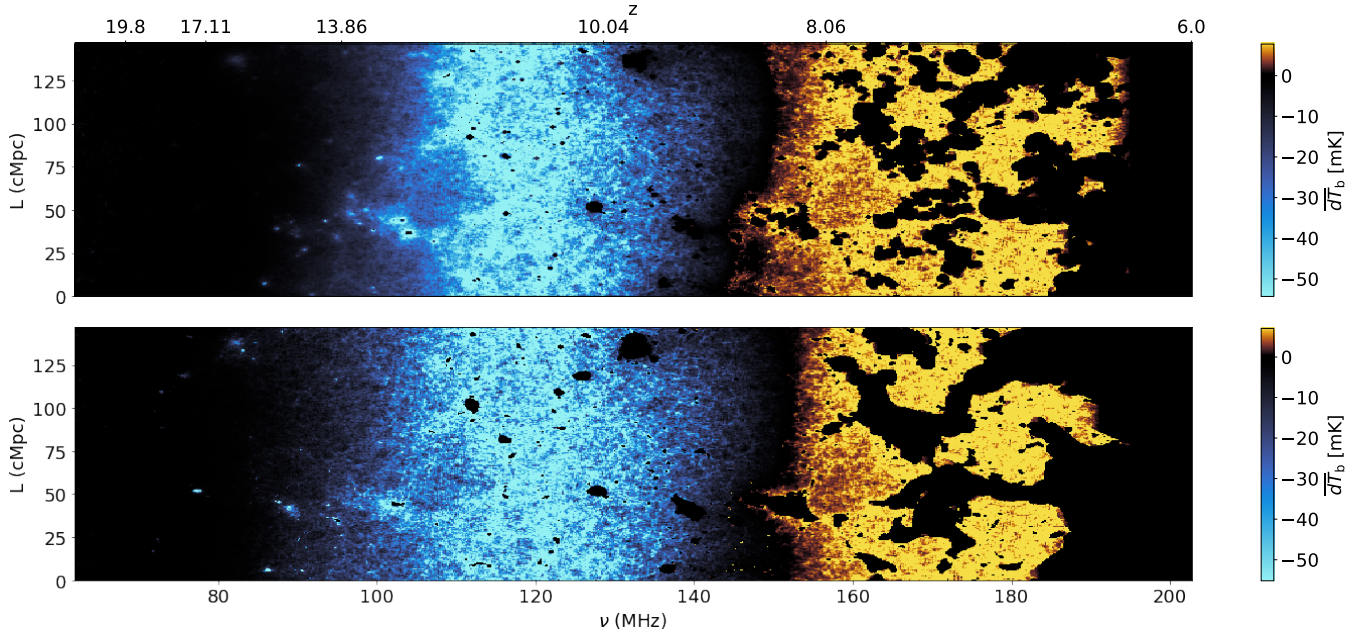


Figure 5. Comparison of lightcone maps for the differential brightness temperature from BEoRN (top) and 21cmFAST (bottom). RSD are not included. Blue and yellow coloured pixels correspond to regions dominated by absorption ($dT_b < 0$) and emission ($dT_b > 0$), respectively. The black patches represent the ionised bubbles ($dT_b = 0$). As illustrated, these bubbles merge and fill the universe by the time it reaches $z \sim 6$.

ionised bubbles (interpreted as being the mean free path of ionising photons) is set to the default value of $R_{\max} = 50$ Mpc. The stellar-to-halo-mass relation in 21cmFAST is parameterised as a power law, followed by an exponential cutoff towards small scales (see eq. 2 in Park et al. 2019). We set its normalisation to $f_{*,10} = 0.02$, the power law index to $\alpha_* = 0.5$, and the turnover mass to $M_{\text{turn}} = 10^9 M_\odot$. We furthermore assume a UV photon number of $N_{\gamma,uv} = 5000$ as well as a flat escape fraction with normalisation $f_{\text{esc},10} = 0.25$. The X-ray spectral index is set to $\alpha_X = 1.5$, and the X-ray flux normalisation to $L_X = 3.4 \times 10^{40} \text{erg.s}^{-1} \cdot M_\odot^{-1} \cdot \text{yr}$, in the energy range $E_{\min} = 500\text{eV}$, $E_{\max} = 2\text{keV}$. Finally, we turn off redshift space distortions for the comparison.

Next to the default 21cmFAST simulation specified above, we rerun 21cmFAST, assuming the exact same setup (with identical random seed), this time turning on the embedded halo algorithm (USEHALOS = 1). The created halo catalogues as well as the corresponding dark matter density fields are then used as input files for BEoRN. This allows for a comparison based on the same realisation of the density and source fields minimising the impact of cosmic variance.

3.1 Global quantities

To ensure consistency of the global quantities, such as the mean IGM temperature (\bar{T}_k), the ionization history (\bar{x}_{HII}), and the sky-averaged 21-cm signal ($\overline{dT_b}$) between the two codes, we fit the different stellar-to-halo relation (f_*) and escape fraction (f_{esc}) to the model of 21cmFAST and recalibrate a few selected parameters. The best fit for $f_*(M)$ is obtained assuming the values $f_{*,0} = 0.02$, $\gamma_1 = -0.5$, $\gamma_2 = -0.5$, $\gamma_3 = 1.4$, $\gamma_4 = -4$, $M_p = 10^{10} M_\odot$, and $M_t = 4 \times 10^8 M_\odot$ in Eq. (5). The escape fraction of ionising photons and the X-ray flux are parameterised in the same way in both codes. We hence set $f_{\text{esc},10} = 0.25$ and $\alpha_{\text{esc}} = 0$ in

Eq. (11) as well as $c_X = 3.4 \times 10^{40} \text{erg.s}^{-1} \cdot M_\odot^{-1} \cdot \text{yr}$, $\alpha_X = 1.5$, $E_{\min} = E_{\min,\text{norm}} = 500\text{eV}$ and $E_{\max} = E_{\max,\text{norm}} = 2\text{keV}$ in Eq. (9).

Finally, we assume a flat Lyman- α spectral index $\alpha_s = 0$ in Eq. (8), instead of the piece-wise power-law used in 21cmFAST. We then fine-tune N_α , f_X , and N_{ion} until we exactly match the global quantities $\bar{T}_k(z)$, $\bar{x}_{\text{HII}}(z)$, and $\overline{dT_b}(z)$.

In Fig. 4, we present the outcome of the aforementioned process. The 21cmFAST predictions are illustrated as thick lines, while the BEoRN data are shown as thin lines. The bottom-central panel of Fig. 4 shows the ionisation histories $x_{\text{HII}}(z)$, which agree well between the two codes for the same number of ionising photons per baryon in stars: $N_{\text{ion}} = N_{\gamma,uv} = 5000$. To match the mean kinetic gas temperature (shown in the top-central panel of Fig. 4), we set the X-ray normalisation to $f_X = 0.8$. We speculate that this mismatch is related to the different treatment of $f_{X,h}$ in the two codes. To achieve agreement in the global signal between redshifts $11 < z < 18$, we adjust the number of Lyman- α photons per stellar baryon N_α . The best match between the two curves was obtained for $N_\alpha = 3000$. Note that the global signal predicted by BEoRN is steeper during Lyman- α coupling ($13 < z < 18$) than the one from 21cmFAST. We speculate that this variation is caused by differences in the star formation rate densities resulting from the collapse fraction and halo fields.

3.2 Power spectrum and lightcone images

After ensuring that the global quantities agree, we compare the power spectra between the two codes. The spherically averaged power spectrum $P_{\text{tot}}(k)$ of the dT_b fluctuations is defined as

$$\langle dT_b(k) dT_b^*(k') \rangle = (2\pi)^3 \delta^{3D}(k - k') |\overline{dT_b}|^2 P_{\text{tot}}(k), \quad (20)$$

where δ^{3D} is the three dimensional Dirac delta. Throughout the paper we express the results in terms of the 'dimensionless' power spectrum $\Delta_{\text{tot}}^2 = k^3 P_{\text{tot}}(k)/2\pi^2$ which only depends on units of $[\text{mK}]^2$.

In the rightmost panel of Fig. 4, we plot the dimensionless power spectra as a function of redshift z for three different k -values from BEoRN (thin lines) and 21cmFAST (thick lines). The results from both codes show similar features, with three distinct peaks at large scales ($k = 0.09 \text{ Mpc}^{-1}$) representing the epochs of Lyman- α coupling, heating, and reionisation, respectively. At smaller scales ($k = 0.42$ and $0.94, \text{ Mpc}^{-1}$), the Lyman- α and heating peaks merge, but the reionisation peak remains distinct.

The comparison between BEoRN and 21cmFAST reveals some similarities and differences. At very high redshifts ($z > 14$), BEoRN predicts a lower power spectrum compared to 21cmFAST, with a difference of up to one order of magnitude, especially at small scales. During the epochs of Lyman- α coupling and heating ($8 < z < 14$), the two codes agree reasonably well, with a relative difference of about a factor of 2 or less. During reionisation ($z < 8$ or $x_{\text{HII}} > 0.2$), BEoRN shows significantly less power at large scales while the small scales are similar to the results of 21cmFAST.

In Fig. 5 we provide lightcone maps of dT_b field generated with BEoRN (top) and 21cmFAST (bottom). The slice thickness is 0.49 cMpc which corresponds to the side-length of one pixel. The blue and yellow colours show regions visible in absorption and emission, respectively. The black patches which grow in size towards lower redshifts correspond to the ionised bubbles.

Comparing the two maps of Fig. 5 we see that ionizing patches form at similar locations, but differences in their morphology are visible. In general, 21cmFAST exhibits larger and smoother bubbles compared to the predictions from BEoRN. This general observation is in qualitative agreement with earlier findings that semi-numerical schemes predict larger and more connected ionised patches compared to simulations based on radiative transfer calculations (see e.g. Zahn et al. 2011; Majumdar et al. 2014). It also agrees with our earlier findings of the power spectrum where at the largest scales 21cmFAST predicted a significantly higher signal than BEoRN.

In Appendix C we study in more detail the differences between the large-scale power from 21cmFAST and BEoRN. In particular, we suggest that the difference may be caused by the different treatments of the photon mean free path. In 21cmFAST, the mean free path of ionising photons is parameterised through R_{max} , which limits the maximum distance photons can travel. In contrast, the mean free path in BEoRN is an inherent feature of the code, determined by the x_{HII} maps and the bubble size distribution. As demonstrated by Georgiev et al. (2022), reducing the value of R_{max} in 21cmFAST leads to a shift of power from large to small scales, which is in qualitative agreement with the shift observed in Fig. 4. In Appendix C, we furthermore compare our results with those of Davies & Furlanetto (2022), who developed an improved excursion-set method that accounts for the gradual absorption of ionising photons, rather than treating the mean free path as a sharp barrier (as is the case with R_{max}). We find a better match between BEoRN and the results from Davies & Furlanetto (2022) compared to the standard R_{max} -method implemented in 21cmFAST.

4 RESULTS

In this section, we present new simulations of the 21-cm signal at cosmic dawn based on BEoRN combined with a large N -body run. The simulations are calibrated against high-redshift observations of the ultraviolet (UV) luminosity functions, the global ionisation

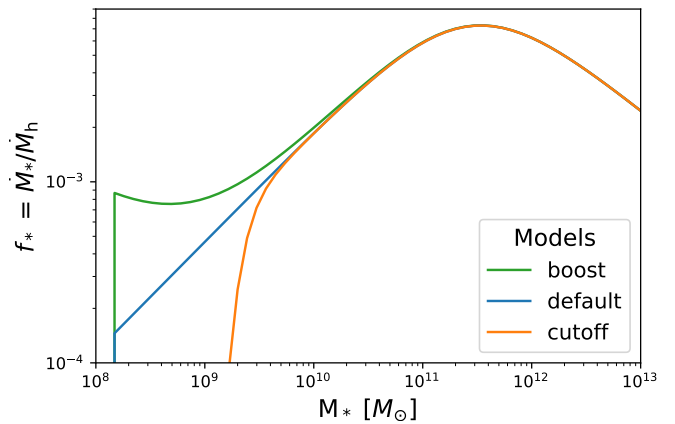


Figure 6. Stellar-to-halo mass relation for the three benchmark models characterised by a boost (green), a power-law decrease (blue, default model), and a cutoff (orange) towards small halo masses. We set $f_* = 0$ below the minimum halo mass $M_h = 1.47 \times 10^8 M_\odot$ of the simulation. The functional form of f_* is given in Eq. 5 the parameter values are provided in Table 1.

fraction, and the CMB optical depth measurement. We focus on three benchmark models with different astrophysical source parameters. While they all agree with the high-redshift observations considered here, they provide very different predictions regarding the 21-cm signal.

4.1 N-body simulation

To obtain converged 21-cm power spectra during reionisation, a large-scale simulation volume with box-size of at least $\sim 150 \text{ cMpc}$ is required (Iliev et al. 2014; Giri et al. 2023). Additionally, the resolution has to be sufficiently high to include haloes down to the atomic cooling limit (i.e. approximately at $M_h \sim 10^8 M_\odot$) as they are believed to be the first sites of star formation. Accounting for these requirements, we run a gravity-only N -body simulation for a 147 cMpc box with 2048^3 particles, yielding a particle mass of $M_{\text{part}} = 1.47 \times 10^7 M_\odot$. We use the N -body code Pkdgrav3 (Potter et al. 2017) initialising the simulation at $z = 150$ based on a transfer function from CAMB (Lewis et al. 2000) with cosmological parameters specified in Sec. 1. The halo catalogue is obtained with the on-the-fly friends-of-friend halo finder embedded in Pkdgrav3 assuming a linking length of 0.2 times the inter-particle distance. We include haloes with at least 10 DM particles in our catalogue, which correspond to a minimum halo mass of $M_{h,\text{min}} = 1.47 \times 10^8 M_\odot$. The density fields and halo catalogues are saved every 10 Myr between $z = 25$ and 6. More details about the simulation and the halo catalogue can be found in Appendix D. We generate velocity fields from the density maps following the method outlined in (Mesinger et al. 2011). They are used in the analysis to include RSD effects.

4.2 Constraints from luminosity function

The UV luminosity function ϕ_{UV} is a measure of the number density of galaxies at a given redshift, observed in a specific rest frame UV frequency band. It is determined using photometric data from telescopes, such as Spitzer (Bowler et al. 2020), the Hubble Space Telescope (McLure et al. 2013; McLeod et al. 2016; Livermore et al. 2017; Ishigaki et al. 2018; Atek et al. 2018; Oesch et al. 2018; De Barros et al. 2019; Rojas-Ruiz et al. 2020; Bouwens et al. 2021), and,

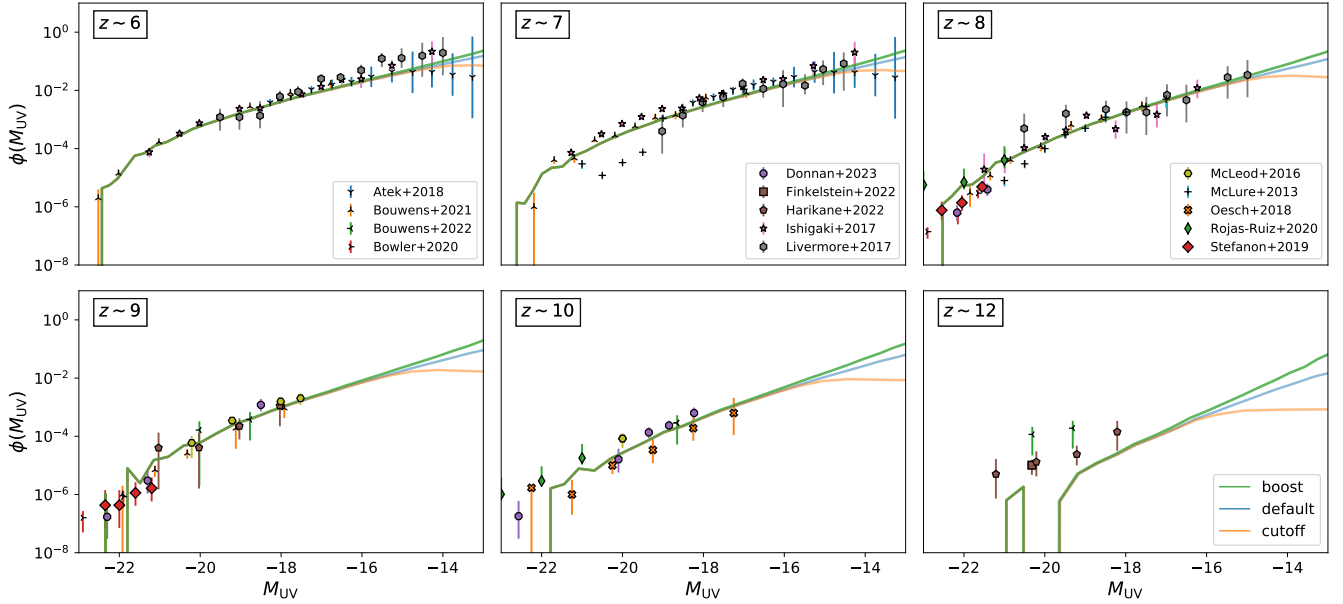


Figure 7. Luminosity function ϕ_{UV} [$\text{mag}^{-1} \text{Mpc}^{-3}$], at different redshifts. The observational data points (with 1σ error bars) have been collected from the literature (McLure et al. 2013; McLeod et al. 2016; Livermore et al. 2017; Ishigaki et al. 2018; Atek et al. 2018; Oesch et al. 2018; De Barros et al. 2019; Bowler et al. 2020; Rojas-Ruiz et al. 2020; Bouwens et al. 2021; Bouwens et al. 2022; Finkelstein et al. 2022; Donnan et al. 2022; Harikane et al. 2023). The three solid lines correspond to the *default* (blue), *cutoff* (orange), and *boost* (green) model presented in the text. They are characterised by different shapes of the stellar-to-halo ratio at the low-mass end.

Table 1. Specific parameters for the three models. γ_3 , γ_4 and M_t control the low mass tail of f_* (Eq. 5). $f_{\text{esc},0}$ and α_{esc} determine the amplitude and power-law slope of the escape fraction of ionising photons (Eq. 11). f_X controls the intensity of X-ray radiation (Eq. 9). The three models share common parameters that are not displayed in the table. It includes $f_{*,0} = 0.02$, $\gamma_1 = 0.49$, $\gamma_2 = -0.61$, $M_p = 2.8 \times 10^{11} M_\odot$, $c_X = 10^{40.5} \text{erg s}^{-1} \text{yr} M_\odot^{-1}$, $\alpha_X = 1.5$, $E_{\text{min}} = 500\text{eV}$, $E_{\text{max}} = 2000\text{eV}$, $N_{\text{alpha}} = 9690$, $\alpha_s = 0$, and $N_{\text{ion}} = 5000$ (Eqs. 5.8, and 9).

Model	γ_3	γ_4	$M_t [M_\odot]$	$f_{\text{esc},0}$	α_{esc}	f_X
<i>boost</i>	1	1	7.35×10^8	0.26	0	5
<i>default</i>	0	0	0	0.3	0.2	1
<i>cutoff</i>	4	-4	1.47×10^9	0.43	0.5	0.1

more recently, the James Webb Space Telescope (Bouwens et al. 2022; Finkelstein et al. 2022; Donnan et al. 2022; Harikane et al. 2023). The UV luminosity function provides an independent way to constrain astrophysical source parameters that are relevant for the 21-cm signal. Note that these source properties are degenerate with the nature of dark matter (e.g. Rudakovskiy et al. 2021; Dayal & Giri 2023). We defer the exploration of dark matter models to the future.

Two ingredients are essential to model the UV luminosity function: the halo mass function, and a model to populate haloes with galaxies. Following Sabti et al. (2021), we express ϕ_{UV} as

$$\phi_{UV} = \frac{dn}{dM_h} \frac{dM_h}{dM_{UV}} \quad (21)$$

where dn/dM_h is the halo mass function from our simulation. The absolute UV magnitude (M_{UV}) is a dimensionless quantity related to

the UV luminosity L_{UV} [erg s^{-1}] via

$$\log_{10} \left(\frac{L_{UV}}{\text{erg s}^{-1}} \right) = 0.4 \times (51.63 - M_{UV}). \quad (22)$$

Finally, the UV luminosity is related to the star formation rate via

$$\dot{M}_* = \kappa_{UV} \times L_{UV} = \frac{m_p}{N_{UV} \times E_{UV}} L_{UV}, \quad (23)$$

where $\kappa_{UV} = 1.15 \times 10^{28} [\text{M}_\odot \text{yr}^{-1} \text{erg}^{-1} \text{s}]$ is a conversion factor from Sun & Furlanetto (2016).

Using our halo catalogues, we can solve Eqs. (21-23) to obtain the UV luminosity function at various redshifts. We tune f_* to match observational data from HST, Spitzer, and JWST at different redshifts. Our best-fitting parameters are $f_{*,0} = 0.05$, $\gamma_1 = 0.49$, $\gamma_2 = -0.61$, and $M_p = 2.8 \times 10^{11} M_\odot$. It is worth noting that γ_1 , γ_2 , and M_p have the same value as in Mirocha et al. (2016).

The low mass end of f_* remains unconstrained due to the limited data at the faint end of ϕ_{UV} . To explore the impact of these faint galaxies on the 21-cm signal, we build three different models (*boost*, *default*, and *cutoff*) with different shapes of f_* at small halo masses. These models are similar to the *floor*, *dpl*, and *steep* models from Mirocha et al. (2016). The functional shape of their stellar-to-halo mass relation (f_*) are shown in Fig. 6. The characteristics of each model are summarised below:

- *Boost*: In this extreme model, f_* starts to gradually flatten and increase again towards small halo masses below $10^{10} M_\odot$ (see green line in Fig. 6). We obtain this behaviour by setting $\gamma_3 = 1$, $\gamma_4 = 1$, and $M_t = 7.35 \times 10^8 M_\odot$. The unusual small-scale behaviour of f_* can be motivated by efficient Population III star formation in the very first galaxies.
- *Default*: In this model, f_* continues to decrease as a power law down to the smallest star-forming haloes (see blue line in Fig. 6).

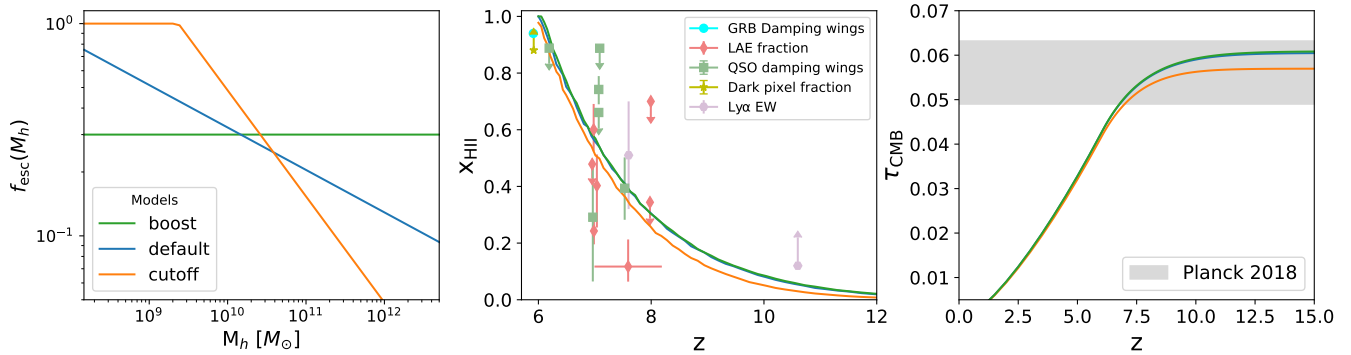


Figure 8. *Left:* Escape fraction of ionising photons f_{esc} , as a function of halo mass. We adjust the shape of f_{esc} to compensate for the different shapes of f_* at small masses in order to obtain similar reionisation history in the three models. *Middle:* Mean ionisation fraction history in the three models (solid lines). We gathered the observational constraints from the literature (Ouchi et al. 2010; Mortlock et al. 2011; Ono et al. 2011; Schroeder et al. 2012; Tilvi et al. 2014; Pentericci et al. 2014; Totani et al. 2016; ?; Mason et al. 2018; Hoag et al. 2019; ?; Jung et al. 2020; Bruton et al. 2023). *Right:* CMB Thomson scattering optical depth. The shaded region corresponds to the value inferred by Planck 2018 with 1σ uncertainty.

The corresponding model parameters are $\gamma_3 = 0$ and $\gamma_4 = 0$. Such a model reflects a continuous suppression effect of feedback mechanisms down to the atomic cooling limit.

- *Cutoff:* This model is characterised by a sharp cutoff in f_* , with no star-formation in haloes below $10^9 M_\odot$ (orange line in Fig. 6). The functional shape is given by the parameters $\gamma_3 = 4$, $\gamma_4 = -4$, and $M_t = 1.47 \times 10^9 M_\odot$. The model represents a situation where feedback effects completely shut down star formation in smaller dwarfs due to e.g. the ejection of gas outside of the potential well preventing any further star formation.

For all three models, the stellar-to-halo mass relation is truncated at $M_h = 1.47 \times 10^8 M_\odot$ corresponding to the resolution limit of our simulation. Note that this roughly agrees with the atomic cooling limit below which gas cooling becomes inefficient (as it relies on the presence of H_2 molecules).

In Fig. 7 we plot the observed UV luminosity functions (data points) together with our predictions from Eq. (21). The three benchmark models are shown in green (boost), blue (default), and orange (cutoff). All three provide a good fit to the data across all redshifts, differing only at magnitudes where no data is available. The noise in our curves at low magnitudes ($M_{\text{UV}} < -20$), more pronounced towards the highest redshift, is explained by the small number of large haloes in our simulation (see the error bars in the HMF plot in Fig. D). Given the simplicity of the model, the agreement between theory and observations is surprisingly good. However, a visible discrepancy starts to appear at $z = 12$, where the data points lie above the curves. This appearing tension might point towards a redshift dependence in the stellar-to-halo mass relation.

4.3 Constraints from reionisation

In our framework, the timing and duration of reionisation are controlled by the product of three quantities: $f_* \times f_{\text{esc}} \times N_{\text{ion}}$. We have determined f_* for the three models in Sec. 4.2 but the values of f_{esc} and N_{ion} remain yet to be defined. Following Park et al. (2019), we set the number of ionising photons per stellar baryons to $N_{\text{ion}} = 5000$. We then vary the f_{esc} to guarantee the ionisation process to end at $z \sim 6$.

For the *default* model, we set the parameters for the escape fraction (see Eq. 11) to $f_{\text{esc},0} = 0.3$, and $\alpha_{\text{esc}} = 0.2$. This corresponds to a

functional form in qualitative agreement with results from hydrodynamical simulations (Kimm et al. 2017). For the *cutoff* model, we assume a steeper function with $f_{\text{esc},0} = 0.43$ and $\alpha_{\text{esc}} = 0.5$ compensating the lack of small star-forming haloes. The *boost* model finally requires a small escape fraction to counteract the high star formation efficiency at small halo masses. We assume a flat function with $f_{\text{esc},0} = 0.26$, and $\alpha_{\text{esc}} = 0$.

In Fig. 8 we plot the escape fraction (left), the global ionisation fraction (centre), and the CMB Thomson scattering optical depth (right) for all three benchmark models. The evolution of the *default*, *boost*, and *cutoff* models are illustrated by green, blue, and orange lines, respectively.

For the global ionisation fraction shown in the middle panel of Fig. 8, we have added observational data from the literature (coloured data points). The measurements come from observations of Lyman- α emitters (Ouchi et al. 2010; Ono et al. 2011; Tilvi et al. 2014; Pentericci et al. 2014; Mason et al. 2018; Hoag et al. 2019), Lyman- α equivalent widths (Jung et al. 2020; Bruton et al. 2023), dark pixel fractions (McGreer et al. 2014), as well as GRBs and QSOs damping wings (Mortlock et al. 2011; Schroeder et al. 2012; Totani et al. 2016; Bañados et al. 2018; Āurovčíková et al. 2020). While they do not all agree with each other, they nevertheless provide a consistent picture of an ionisation history between $z \sim 10$ and 6 which is well reproduced by our benchmark models.

In the rightmost panel of Fig. 8, we indicate the Thomson optical depth measured from the Planck 2018 data (Planck Collaboration et al. 2020). This quantity constrains the integrated history of reionization (see e.g. eq. 12 in Bianco et al. 2021a). The predictions from our three benchmark models are within the 1σ contour (grey band).

4.4 Fixing the remaining parameters

We have now fixed all the parameters connected to pre-reionisation observations. The Lyman- α and X-ray fluxes remain to be specified. To match the Population II stellar model from (Barkana & Loeb 2005), we set the number of Lyman- α photons per stellar baryons to $N_\alpha = 9690$. We assume the spectra of Lyman- α radiation to be flat ($\alpha_s = 0$).

For the X-ray normalisation, we follow (Park et al. 2019) and normalize the flux to $c_X = 10^{40.5} \text{ erg s}^{-1} \text{ yr } M_\odot^{-1}$, in the energy

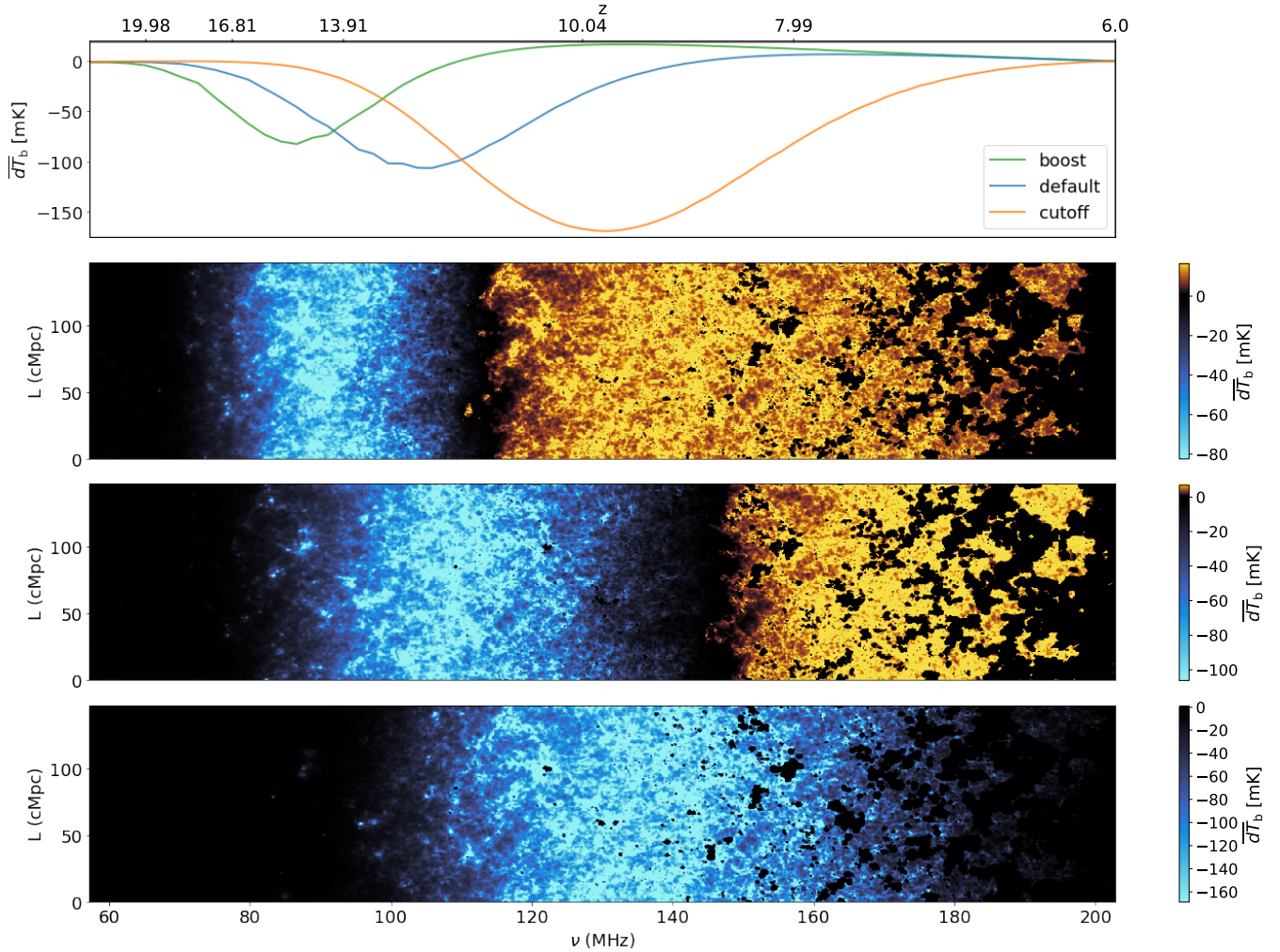


Figure 9. *Upper panel:* Mean differential brightness temperature $\overline{dT_b}$ for the *boost* (green), *default* (blue), and *cutoff* model (orange). *Lower three panels:* Lightcone images showing brightness temperature slices (dT_b) as they evolve with time. RSD are included. The three images correspond to the *boost*, *default*, and *cutoff* models (from top to bottom). The blue colour indicates regions where $dT_b < 0$ (signal in absorption). The yellow colour denotes cells of the IGM that are heated above the CMB temperature, leading to a positive value of dT_b (signal in emission). The black areas correspond to a lack of signal. The appearing patches on the right-hand side of the lightcone images indicate ionised bubbles.

range defined by $E_{\min} = 500$ eV, $E_{\max} = 2$ keV, with a power-law index $\alpha_X = 1$. By doing so, we are assuming that high-mass X-ray binaries (HMXBs) are the dominant sources of X-ray radiation during the entire heating and reionisation period and that soft X-rays with energy below 500 eV are absorbed in the interstellar medium. These parameters are consistent with the simulations from (Fragos et al. 2013; Das et al. 2017). However, the true normalisation and shape of the X-ray spectrum emitted by high redshift galaxies remain highly uncertain. Therefore, we select different values of f_X for our three benchmark models. In the *cutoff* model, f_X is set to 0.1, which corresponds to a rather inefficient heating scenario (similar to what is assumed in Mirocha et al. 2016). For the *default* model, we assume $f_X = 1$, our default assumption for the X-ray flux. In the *boost* model, f_X is set to 5 which means that the IGM is assumed to be very efficiently heated by X-ray sources.

4.5 Resulting 21-cm signal

Given the astrophysical assumptions discussed above, we now look at the simulations of the 21-cm signal predicted by our three benchmark models. We first investigate the global signal and the corresponding light-cone maps in the following subsection. Later we study the corresponding power spectra that are expected to be observed by radio interferometers.

4.5.1 Global signal and lightcone images

The sky-averaged differential brightness temperature $\overline{dT_b}(z)$ or global signal along with the lightcone maps of the three benchmark models are illustrated in Fig. 9. The different stages of cosmic dawn and epoch of reionisation are clearly visible in the 21-cm signal lightcone maps shown in the bottom three rows. Regions in blue and yellow represent the signal seen in absorption and emission respectively. Black regions correspond to no 21-cm signal. The black patches at the low redshift end correspond to ionised bubbles cre-

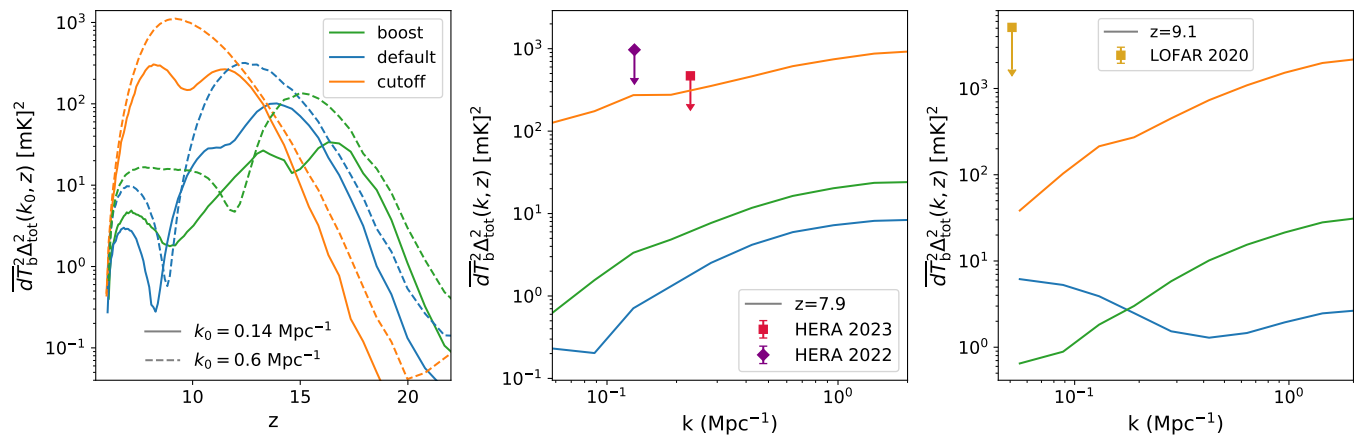


Figure 10. *Left:* Dimensionless power spectrum of the dT_b field as a function of redshift, for the three models - *default*, *cutoff* and *boost* respectively in green, blue and orange. RSD are included. Solid and dashed lines correspond respectively to the Fourier modes $k = 0.14 \text{ Mpc}^{-1}$ and $k = 0.6 \text{ Mpc}^{-1}$. *Middle:* Dimensionless power spectrum at redshift $z = 7.9$, as a function of scale k . The red square and purple diamond are the best HERA upper limits (The HERA Collaboration et al. 2022b, 2023). *Right:* Dimensionless power spectrum at redshift $z = 9.1$, as a function of scale k . The yellow square is the best LOFAR upper limit at this redshift (Mertens et al. 2020).

ated due to the reionisation process. The main coloured areas can be directly connected to the global signal plotted in the top panel.

The Lyman- α coupling epoch marks the beginning of the cosmic dawn. In the three models, the emission of Lyman- α photons drives the spin temperature to the kinetic temperature T_k and leads to a characteristic absorption trough. This trough is seen at $z \sim 15$, 12.2 and 9.7 with minima values of $dT_b \sim -82.4$, -106.2 and -168.8 mK , respectively in the *boost*, *default* and *cutoff* models. These differences in the timing of the absorption trough illustrate the sensitivity of the high redshift dT_b to the tail of the SFE for small haloes with masses between $10^8 M_\odot$ and $10^{10} M_\odot$. During this pre-heating stage, the gas temperature T_k is significantly lower than T_{CMB} , and hence $dT_b < 0$. The transition is visible in the lightcone maps with the colour transitioning from black to blue. Note that the three models are far from the low-frequency band of EDGES observation (Bowman et al. 2018), which detected an absorption trough centred between $z \sim 20$ and $z \sim 15$. This hints that there is a tension between the EDGES observation and the UV luminosity function data set. As already shown by (Mirocha & Furlanetto 2019), fitting simultaneously the UV luminosity function and the timing of the dip of the EDGES signal can only be achieved by a dramatic increase of f_* in minihaloes (similar to our *boost* model, but even more extreme).

The next stage of our Universe observed by the 21-cm signal is known as the epoch of heating. During this stage, X-ray photons cause an increase in the T_k of the gas. If T_k rises above the CMB temperature, the signal is observed in emission ($dT_b > 0$). We see this epoch as yellow regions in the lightcone maps of Fig. 9. Heating is triggered efficiently in the *boost* and *default* models, due to both the values of f_X and the high SFE at small halo masses. In the *cutoff* model, the mean T_k never goes above T_{cmb} . Such a signal corresponds to a “cold reionisation” scenario, in which ionised bubbles grow surrounded by a cold neutral IGM. Our results for the *cutoff* model are consistent with those from (Mirocha et al. 2016), who assumed similarly inefficient heating parameters and obtained the same type of global signal.

During the epoch of reionisation, UV photons start to ionise the intergalactic medium (IGM) forming bubbles around sources. These ionised bubbles appear as black patches in the lightcone images and start to grow at around $z \sim 10$, percolating around $z \sim 8$ until they

fill the entire box volume by $z \sim 6$. The morphology of ionisation depends on the halo distribution, the star-formation efficiency, the UV photon production, and the escape fraction. Note that the three models show similar morphologies of their ionisation maps. This can be explained by the fact that we have adjusted the shape of the escape fraction to compensate for the differences in star-formation efficiency.

4.5.2 Power Spectrum

In the leftmost panel of Fig. 10, we show the redshift evolution of the dimensionless power spectra of the dT_b fields for the three benchmark models following the same colour scheme as before. Solid and dashed lines correspond to the different wave modes $k = 0.14 \text{ Mpc}^{-1}$ and $k = 0.6 \text{ Mpc}^{-1}$. As expected, the three spectra display distinct peaks and troughs, which correspond to the epochs when the dT_b field is dominated by fluctuations of the Lyman- α coupling (x_α), the temperature (T_k), and the ionisation (x_{HII}) field.

The Lyman- α peak occurs roughly at the midpoint of Lyman- α coupling, when dT_b fluctuates between regions still coupled to the CMB ($dT_b = 0$), and regions in absorption coupled to the kinetic temperature ($dT_b < 0$). It is located at $z \sim 16.5$, 14, 11.5 in the *boost*, *default*, and *cutoff* models, respectively. The Lyman- α peak is followed by a gap, which occurs when the mean dT_b is minimal (respectively at $z \sim 14.6$, 11.6, 9.7). This is due to the negative cross-correlation between the x_α and T_k fields.

After that point, the three models can be divided into two categories: (i) In the *boost* and *default* models, the spectra have a heating peak. It occurs roughly when the mean dT_b is halfway from reaching its maximum positive value. The peak is followed by a second trough when the mean dT_b is maximal. The spectra then hit a third peak, when respectively 50% and 60% of the universe is ionised. (ii) In the *cutoff* model, the spectrum has no heating peak. Heating is inefficient and proceeds very slowly: dT_b fluctuates between cold regions with negative values and growing ionised regions with no signal ($dT_b = 0$). The power spectrum hits a single peak when 30% of the universe is ionised. It reaches very high values ($\sim 3 \times 10^2 \text{ mK}^2$ at $k = 0.14 \text{ Mpc}^{-1}$), which reflects the strong contrast between neutral regions with $dT_b \sim -150 \text{ mK}$ and ionised region with $dT_b = 0 \text{ mK}$.

In the middle and rightmost panels of Fig. 10, we plot the power spectra as a function of k -modes at the distinct redshift values of $z = 7.9$ and $z = 9.1$. Next to our results, we plot the current upper limits on the 21-cm power spectrum HERA (The HERA Collaboration et al. 2022b, 2023, which are shown as red square and purple diamond markers respectively), and LOFAR observations (Mertens et al. 2020, which is shown as a yellow square). While the upper limits are still significantly higher than the bulk of predictions, the *cutoff* model comes close to the limits from HERA (intersecting with the 1σ error bar). This finding is in agreement with previous work (The HERA Collaboration et al. 2022a; Ghara et al. 2020, 2021; Greig et al. 2021a) in which cold reionisation scenarios were shown to be disfavoured.

5 CONCLUSIONS

In the near future, radio interferometers such as the Square Kilometre Array (SKA) telescope are expected to provide first observations of the 21-cm signal from the epoch of reionisation and cosmic dawn. These observations will yield new insights into the properties of the very first galaxies and they will help stress-testing the Λ CDM model in a currently un-probed regime.

In order to interpret and understand the 21-cm signal at cosmic dawn, fast and accurate prediction methods are required. In this paper we introduce the *Bubbles during the Epoch of Reionisation Numerical simulator* (BEoRN), a new simulation framework to produce maps and lightcone images of the 21-cm signal. BEoRN is designed as a user-friendly and modular, open-source code written entirely in Python. It can produce 3-dimensional maps of the 21-cm brightness temperature dT_b from cosmic dawn to reionisation, including Lyman- α coupling, heating, and ionisation of neutral hydrogen by galaxies.

BEoRN is based on the concept of overlying flux profiles around sources and follows the basic methodology developed in Schneider et al. (2021, 2023). The method works by pre-calculating individual profiles of Lyman- α , X-ray, and ionising photon fluxes for different halo masses, assuming a given stellar-to-halo mass relation and including photon redshifting as well as look-back effects due to the finite speed of light. The resulting profiles are painted on a 3-dimensional grid using halo positions and density fields from a N -body simulation. Overlaps of ionising bubbles are dealt with by re-distributing excess photons at the bubble boundaries.

We validate BEoRN by comparing it to the semi-numerical algorithm 21cmFAST. The two codes agree reasonably well for all relevant redshifts and k -modes (as shown in Figs. 4 and 5). However, during the epoch of bubble growth, BEoRN predicts a larger number of smaller, more irregular ionised patches compared to 21cmFAST. This results in a significant difference in amplitude of the power spectrum at large scales, in qualitative agreement with earlier comparisons between semi-numerical codes and radiative transfer simulations (Zahn et al. 2011; Majumdar et al. 2014).

After validating the code, we run a large N -body simulation (with a box length of 147 cMpc and $N = 2048^3$ particles) using the resulting density grids and the halo catalogues as input fields for BEoRN. We study three benchmark models with vastly different choices for the astrophysical parameters, that are, however, all selected to reproduce recent observations of the UV luminosity functions, the global ionisation fraction, and the Thomson optical depth measurement. The three benchmark models are characterised by different stellar-to-halo relations (f_*) at small halo masses, different escape fractions for the ionising photons, and different normalisation factors for the emitted

X-ray flux. They lead to strongly different 21-cm signals ranging from a cold reionisation scenario with a deep absorption trough at late times to an emission-dominated scenario with only a shallow absorption trough at high redshift. The global signal evolution and lightcone images of each benchmark model are shown in Fig. 9.

In this work, we have focused on the global effects of feedback, specifically Lyman-Werner and radiative feedback, on star formation within dark matter haloes. However, it is important to note that this feedback process is expected to vary with position and time (e.g., Dixon et al. 2016; Hutter et al. 2021). We have incorporated these calculations into BEoRN, and a comprehensive analysis will be presented in a forthcoming publication.

The results from our three benchmark runs confirm that current observations from the period of reionisation and cosmic dawn allow for a large variety of different scenarios that can be studied with the 21-cm global and clustering signal. This shows that upcoming radio experiments will provide crucial support for our understanding of star and galaxy formation during the first billion years after the Big Bang.

ACKNOWLEDGEMENTS

We thank Douglas Potter and Joachim Stadel for helping with the Pkdgrav3 code. We thank Raghunath Ghara and Garrelt Mellema for useful discussions. TS would like to express his gratitude to Deniz Soyuer for his proofreading, and for the daily inspiration he provides. This study is supported by the Swiss National Science Foundation via the grant PCEFP2_181157. Nordita is supported in part by NordForsk.

DATA AVAILABILITY

The data underlying this article will be shared on reasonable request to the corresponding author.

REFERENCES

- Alvarez M. A., Abel T., 2012, *The Astrophysical Journal*, 747, 126
- Atek H., Richard J., Kneib J.-P., Schaerer D., 2018, *Monthly Notices of the Royal Astronomical Society*, 479, 5184
- Bañados E., et al., 2018, *Nature*, 553, 473
- Barkana R., Loeb A., 2005, *The Astrophysical Journal*, 626, 1
- Barkana R., Outmezguine N. J., Redigolo D., Volansky T., 2018, *Phys. Rev. D*, 98, 103005
- Behroozi P. S., Wechsler R. H., Conroy C., 2013, *The Astrophysical Journal*, 770, 57
- Behroozi P., et al., 2020, *Monthly Notices of the Royal Astronomical Society*, 499, 5702
- Bianco M., Iliev I. T., Ahn K., Giri S. K., Mao Y., Park H., Shapiro P. R., 2021a, *Monthly Notices of the Royal Astronomical Society*, 504, 2443
- Bianco M., Giri S. K., Iliev I. T., Mellema G., 2021b, *Monthly Notices of the Royal Astronomical Society*, 505, 3982
- Bianco M., et al., 2023, arXiv preprint arXiv:2304.02661
- Bond J. R., Cole S., Efstathiou G., Kaiser N., 1991, *ApJ*, 379, 440
- Bouwens R. J., et al., 2021, *AJ*, 162, 47
- Bouwens R., Illingworth G., Oesch P., Stefanon M., Naidu R., van Leeuwen I., Magee D., 2022, UV Luminosity Density Results at $z > 8$ from the First JWST/NIRCam Fields: Limitations of Early Data Sets and the Need for Spectroscopy (arXiv:2212.06683)
- Bowler R. A. A., Jarvis M. J., Dunlop J. S., McLure R. J., McLeod D. J., Adams N. J., Milvang-Jensen B., McCracken H. J., 2020, *MNRAS*, 493, 2059

- Bowman J. D., Rogers A. E. E., Monsalve R. A., Mozdzen T. J., Mahesh N., 2018, *Nature*, **555**, 67
- Bruton S., Lin Y.-H., Scarlata C., Hayes M. J., 2023, The Universe is at Most 88% Neutral at $z=10.6$ ([arXiv:2303.03419](https://arxiv.org/abs/2303.03419))
- Chatterjee A., Dayal P., Choudhury T. R., Hutter A., 2019, *MNRAS*, **487**, 3560
- Choudhury T. R., Paranjape A., 2018, *Monthly Notices of the Royal Astronomical Society*, 481, 3821
- D'Amico G., Panci P., Strumia A., 2018, *Phys. Rev. Lett.*, 121, 011103
- Das A., Mesinger A., Pallottini A., Ferrara A., Wise J. H., 2017, *MNRAS*, **469**, 1166
- Datta K. K., Mellema G., Mao Y., Iliev I. T., Shapiro P. R., Ahn K., 2012, *Monthly Notices of the Royal Astronomical Society*, 424, 1877
- Davies F. B., Furlanetto S. R., 2022, *Monthly Notices of the Royal Astronomical Society*, 514, 1302
- Dayal P., Giri S. K., 2023, arXiv preprint arXiv:2303.14239
- De Barros S., Oesch P. A., Labbé I., Stefanon M., González V., Smit R., Bouwens R. J., Illingworth G. D., 2019, *MNRAS*, **489**, 2355
- Dekel A., Zolotov A., Tweed D., Cacciato M., Ceverino D., Primack J. R., 2013, *Monthly Notices of the Royal Astronomical Society*, 435, 999
- Dixon K. L., Iliev I. T., Mellema G., Ahn K., Shapiro P. R., 2016, *Monthly Notices of the Royal Astronomical Society*, 456, 3011
- Donnan C. T., et al., 2022, *Monthly Notices of the Royal Astronomical Society*, 518, 6011
- Feng Y., Chu M.-Y., Seljak U., McDonald P., 2016, *Monthly Notices of the Royal Astronomical Society*, 463, 2273
- Fialkov A., Barkana R., 2014, *MNRAS*, **445**, 213
- Fialkov A., Barkana R., Cohen A., 2018, *Phys. Rev. Lett.*, 121, 011101
- Field G. B., 1958, *Proceedings of the IRE*, **46**, 240
- Finkelstein S. L., et al., 2022, *arXiv e-prints*, p. arXiv:2211.05792
- Fiorio C., Gustedt J., 1996, *Theoretical Computer Science*, 154, 165
- Flitter J., Kovetz E. D., 2022, *Phys. Rev. D*, 106, 063504
- Fragos T., et al., 2013, *The Astrophysical Journal*, 764, 41
- Furlanetto S. R., Oh S. P., 2005, *Monthly Notices of the Royal Astronomical Society*, 363, 1031
- Furlanetto S., Zaldarriaga M., Hernquist L., 2004, *The Astrophysical Journal*, 613
- Furlanetto S. R., Peng Oh S., Briggs F. H., 2006, *Physics Reports*, 433, 181
- Garaldi E., Kannan R., Smith A., Springel V., Pakmor R., Vogelsberger M., Hernquist L., 2022, *MNRAS*, **512**, 4909
- Gazagnes S., Koopmans L. V., Wilkinson M. H., 2021, *Monthly Notices of the Royal Astronomical Society*, 502, 1816
- Georgiev I., Mellema G., Giri S. K., Mondal R., 2022, *Monthly Notices of the Royal Astronomical Society*, 513, 5109
- Ghara R., Choudhury T. R., Datta K. K., Choudhuri S., 2017, *Monthly Notices of the Royal Astronomical Society*, 464, 2234
- Ghara R., Mellema G., Giri S. K., Choudhury T. R., Datta K. K., Majumdar S., 2018, *Monthly Notices of the Royal Astronomical Society*, 476, 1741
- Ghara R., et al., 2020, *MNRAS*, **493**, 4728
- Ghara R., Giri S. K., Ciardi B., Mellema G., Zaroubi S., 2021, *MNRAS*, **503**, 4551
- Giri S. K., Mellema G., 2021, *Monthly Notices of the Royal Astronomical Society*, 505, 1863
- Giri S. K., Schneider A., 2022, *Phys. Rev. D*, 105, 083011
- Giri S. K., Mellema G., Dixon K. L., Iliev I. T., 2018a, *Monthly Notices of the Royal Astronomical Society*, 473, 2949
- Giri S. K., Mellema G., Ghara R., 2018b, *Monthly Notices of the Royal Astronomical Society*, 479, 5596
- Giri S., Mellema G., Jensen H., 2020, *Journal of Open Source Software*, 5, 2363
- Giri S. K., Schneider A., Maion F., Angulo R. E., 2023, *Astronomy and Astrophysics*, 669, A6
- Greig B., Trott C. M., Barry N., Mutch S. J., Pindor B., Webster R. L., Wyithe J. S. B., 2021a, *MNRAS*, **500**, 5322
- Greig B., et al., 2021b, *MNRAS*, **501**, 1
- Harikane Y., et al., 2023, *The Astrophysical Journal Supplement Series*, 265, 5
- Hibbard J. J., Mirocha J., Rapetti D., Bassett N., Burns J. O., Tauscher K., 2022, *ApJ*, **929**, 151
- Hoag A., et al., 2019, *The Astrophysical Journal*, 878, 12
- Hotinli S. C., Marsh D. J. E., Kamionkowski M., 2022, *Phys. Rev. D*, 106, 043529
- Hutter A., Dayal P., Yepes G., Gottlöber S., Legrand L., Ucci G., 2021, *MNRAS*, **503**, 3698
- Iliev I., Mellema G., Pen U.-L., Merz H., Shapiro P., Alvarez M., 2006, *Monthly Notices of the Royal Astronomical Society*, 369, 1625
- Iliev I. T., Mellema G., Ahn K., Shapiro P. R., Mao Y., Pen U.-L., 2014, *Monthly Notices of the Royal Astronomical Society*, 439, 725
- Ishigaki M., Kawamata R., Ouchi M., Oguri M., Shimasaku K., Ono Y., 2018, *The Astrophysical Journal*, 854, 73
- Jensen H., et al., 2013, *Monthly Notices of the Royal Astronomical Society*, 435, 460
- Jones D., Palatnick S., Chen R., Beane A., Lidz A., 2021, *ApJ*, **913**, 7
- Jung I., et al., 2020, *ApJ*, **904**, 144
- Kaiser N., 1987, *Monthly Notices of the Royal Astronomical Society*, 227, 1
- Kannan R., et al., 2022, in *American Astronomical Society Meeting Abstracts*, p. 420.01
- Kimm T., Katz H., Haehnelt M., Rosdahl J., Devriendt J., Slyz A., 2017, *MNRAS*, **466**, 4826
- Kolopanis M., et al., 2019, *ApJ*, **883**, 133
- Kovetz E. D., Poulin V., Gluscevic V., Boddy K. K., Barkana R., Kamionkowski M., 2018, *Phys. Rev. D*, 98, 103529
- Lewis A., Challinor A., Lasenby A., 2000, *The Astrophysical Journal*, 538, 473
- Lewis J. S. W., et al., 2020, *Monthly Notices of the Royal Astronomical Society*, 496, 4342
- Lewis J. S. W., et al., 2022, *MNRAS*, **516**, 3389
- Liu A., Parsons A. R., 2016, *MNRAS*, **457**, 1864
- Liu H., Slatyer T. R., 2018, *Phys. Rev. D*, 98, 023501
- Livermore R. C., Finkelstein S. L., Lotz J. M., 2017, *ApJ*, **835**, 113
- Lopez-Honorez L., Mena O., Villanueva-Domingo P., 2019, *Phys. Rev. D*, 99, 023522
- Majumdar S., Mellema G., Datta K. K., Jensen H., Choudhury T. R., Bharadwaj S., Friedrich M. M., 2014, *Monthly Notices of the Royal Astronomical Society*, 443, 2843
- Mao Y., Shapiro P. R., Mellema G., Iliev I. T., Koda J., Ahn K., 2012, *Monthly Notices of the Royal Astronomical Society*, 422, 926
- Maselli A., Ferrara A., Ciardi B., 2003, *Monthly Notices of the Royal Astronomical Society*, 345, 379
- Mashian N., Oesch P. A., Loeb A., 2015, *Monthly Notices of the Royal Astronomical Society*, 455, 2101
- Mason C. A., Treu T., Dijkstra M., Mesinger A., Trenti M., Pentericci L., de Barros S., Vanzella E., 2018, *The Astrophysical Journal*, 856, 2
- McGreer I. D., Mesinger A., D'Odorico V., 2014, *Monthly Notices of the Royal Astronomical Society*, 447, 499
- McLeod D. J., McLure R. J., Dunlop J. S., 2016, *Monthly Notices of the Royal Astronomical Society*, 459, 3812
- McLure R. J., et al., 2013, *MNRAS*, **432**, 2696
- Mellema G., Iliev I. T., Alvarez M. A., Shapiro P. R., 2006a, *New Astronomy*, 11, 374
- Mellema G., Iliev I. T., Pen U.-L., Shapiro P. R., 2006b, *Monthly notices of the royal astronomical society*, 372, 679
- Mellema G., Koopmans L., Shukla H., Datta K., Mesinger A., Majumdar S., 2015, *Advancing Astrophysics with the Square Kilometre Array (AASKA14)*, p. 10
- Mertens F. G., et al., 2020, *Monthly Notices of the Royal Astronomical Society*, 493, 1662
- Mesinger A., Furlanetto S., Cen R., 2011, *Mon. Not. Roy. Astron. Soc.*, 411, 955
- Mineo S., Gilfanov M., Sunyaev R., 2012, *MNRAS*, **419**, 2095
- Mirocha J., 2014, *Monthly Notices of the Royal Astronomical Society*, 443, 1211
- Mirocha J., Furlanetto S. R., 2019, *MNRAS*, **483**, 1980
- Mirocha J., Furlanetto S. R., Sun G., 2016, *Monthly Notices of the Royal Astronomical Society*, 464, 1365

- Mirocha J., Mebane R. H., Furlanetto S. R., Singal K., Trinh D., 2018, *Mon. Not. Roy. Astron. Soc.*, 478, 5591
- Mitridate A., Podo A., 2018, *J. Cosmology Astropart. Phys.*, 2018, 069
- Mortlock D. J., et al., 2011, *Nature*, 474, 616
- Mosbech M. R., Boehm C., Wong Y. Y. Y., 2023, *JCAP*, 03, 047
- Muñoz J. B., Dvorkin C., Cyr-Racine F.-Y., 2020, *Phys. Rev. D*, 101, 063526
- Murray S., Greig B., Mesinger A., Muñoz J., Qin Y., Park J., Watkinson C., 2020, *The Journal of Open Source Software*, 5, 2582
- Nebrin O., Ghara R., Mellema G., 2019, *J. Cosmology Astropart. Phys.*, 2019, 051
- Ocvirk P., et al., 2016, *MNRAS*, 463, 1462
- Ocvirk P., et al., 2020, *Monthly Notices of the Royal Astronomical Society*, 496, 4087
- Oesch P. A., Bouwens R. J., Illingworth G. D., Labbé I., Stefanon M., 2018, *ApJ*, 855, 105
- Ono Y., et al., 2011, *The Astrophysical Journal*, 744, 83
- Ouchi M., et al., 2010, *The Astrophysical Journal*, 723, 869
- Paardekooper J.-P., Khochfar S., Dalla Vecchia C., 2015, *Monthly Notices of the Royal Astronomical Society*, 451, 2544
- Paciga G., et al., 2013, *MNRAS*, 433, 639
- Park J., Mesinger A., Greig B., Gillet N., 2019, *Monthly Notices of the Royal Astronomical Society*, 484, 933
- Pentericci L., et al., 2014, *The Astrophysical Journal*, 793, 113
- Planck Collaboration et al., 2020, *A&A*, 641, A6
- Potter D., Stadel J., Teyssier R., 2017, *Computational Astrophysics and Cosmology*, 4, 2
- Press W., Schechter P., 1974, *Astrophysical Journal*, 187, 425
- Pritchard J. R., Furlanetto S. R., 2006, *Mon. Not. Roy. Astron. Soc.*, 367, 1057
- Pritchard J. R., Furlanetto S. R., 2007, *MNRAS*, 376, 1680
- Reis I., Fialkov A., Barkana R., 2020, *MNRAS*, 499, 5993
- Rojas-Ruiz S., Finkelstein S. L., Bagley M. B., Stevans M., Finkelstein K. D., Larson R., Mechtley M., Diekmann J., 2020, *ApJ*, 891, 146
- Ross H. E., Dixon K. L., Ghara R., Iliev I. T., Mellema G., 2019, *MNRAS*, 487, 1101
- Ross H. E., Giri S. K., Mellema G., Dixon K. L., Ghara R., Iliev I. T., 2021, *Monthly Notices of the Royal Astronomical Society*, 506, 3717
- Rudakovskiy A., Mesinger A., Savchenko D., Gillet N., 2021, *Monthly Notices of the Royal Astronomical Society*, 507, 3046
- Sabti N., Muñoz J. B., Blas D., 2021, *Journal of Cosmology and Astroparticle Physics*, 2021, 010
- Santos M., Ferramacho L., Silva M., Amblard A., Cooray A., 2010, *SimFast21: Simulation of the Cosmological 21cm Signal*, *Astrophysics Source Code Library*, record ascl:1010.025 (ascl:1010.025)
- Sartorio N. S., et al., 2023, *MNRAS*, 521, 4039
- Schaeffer T., Schneider A., 2021, *MNRAS*, 504, 3773
- Schneider A., Giri S. K., Mirocha J., 2021, *Phys. Rev. D*, 103, 083025
- Schneider A., Schaeffer T., Giri S. K., 2023, *Cosmological forecast of the 21-cm power spectrum using the halo model of reionization* ([arXiv:2302.06626](https://arxiv.org/abs/2302.06626))
- Schroeder J., Mesinger A., Haiman Z., 2012, *Monthly Notices of the Royal Astronomical Society*, 428, 3058
- Semelin B., Eames E., Bolgar F., Caillat M., 2017, *Monthly Notices of the Royal Astronomical Society*, 472, 4508
- Sheth R. K., Mo H. J., Tormen G., 2001, *MNRAS*, 323, 1
- Shmueli G., Sarkar D., Kovetz E. D., 2023, *Mitigating the optical depth degeneracy in the cosmological measurement of neutrino masses using 21-cm observations* ([arXiv:2305.07056](https://arxiv.org/abs/2305.07056))
- Shull J. M., van Steenberg M. E., 1985, *ApJ*, 298, 268
- Sitwell M., Mesinger A., Ma Y.-Z., Sigurdson K., 2014, *MNRAS*, 438, 2664
- Sun G., Furlanetto S. R., 2016, *MNRAS*, 460, 417
- Tassev S., Eisenstein D. J., Wandelt B. D., Zaldarriaga M., 2015, *arXiv preprint arXiv:1502.07751*
- The HERA Collaboration et al., 2022a, *The Astrophysical Journal*, 924, 51
- The HERA Collaboration et al., 2022b, *The Astrophysical Journal*, 925, 221
- The HERA Collaboration et al., 2023, *The Astrophysical Journal*, 945, 124
- Thomas R. M., et al., 2009, *Monthly Notices of the Royal Astronomical Society*, 393, 32
- Tilvi V., et al., 2014, *The Astrophysical Journal*, 794, 5
- Totani T., Aoki K., Hattori T., Kawai N., 2016, *Publications of the Astronomical Society of Japan*, 68
- Trac H., Cen R., 2007, *The Astrophysical Journal*, 671, 1
- Trott C. M., et al., 2020, *MNRAS*, 493, 4711
- Ventura E. M., Trinca A., Schneider R., Graziani L., Valiante R., Wyithe J. S. B., 2023, *Monthly Notices of the Royal Astronomical Society*, 520, 3609
- Wouthuysen S. A., 1952, *A.J.*, 57, 31
- Wu K., Otoo E., Shoshani A., 2005, in *Medical Imaging 2005: Image Processing*. pp 1965–1976
- Wyithe S., Geil P., Kim H., 2015, in *Advancing Astrophysics with the Square Kilometre Array (AASKA14)*. p. 15 ([arXiv:1501.04246](https://arxiv.org/abs/1501.04246)), [doi:10.22323/1.215.0015](https://doi.org/10.22323/1.215.0015)
- Zackrisson E., et al., 2020, *Monthly Notices of the Royal Astronomical Society*, 493, 855
- Zahn O., Mesinger A., McQuinn M., Trac H., Cen R., Hernquist L. E., 2011, *Monthly Notices of the Royal Astronomical Society*, 414, 727
- Žurovčíková D., Katz H., Bosman S. E. I., Davies F. B., Devriendt J., Slyz A., 2020, *Monthly Notices of the Royal Astronomical Society*, 493, 4256

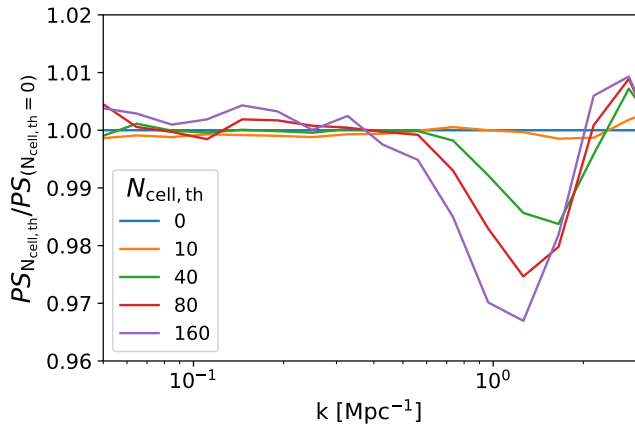


Figure A1. Effect of varying the threshold parameter $N_{\text{cell,th}}$ on the power spectrum of the x_{HII} field. $N_{\text{cell,th}}$ is used to speed up the bubble overlap procedure (see Appendix. A). The y-axis shows the ratio between the PS of the x_{HII} field obtained for different values of $N_{\text{cell,th}}$, with respect to the PS of the fiducial x_{HII} field, obtained for $N_{\text{cell,th}} = 0$. Up to $N_{\text{cell,th}} = 40$ (green curve), the error induced on the power spectrum is less than 1% at the relevant scales ($0.1 \text{ Mpc}^{-1} < k < 1 \text{ Mpc}^{-1}$).

APPENDIX A: SPEEDING UP THE BUBBLE OVERLAP

In the main text, we mentioned that redistributing overionised cells that occur in regions where bubbles overlap can be computationally expensive. The number of ionised "islands" or connected ionised regions varies based on several factors such as the number of haloes, the astrophysical model, the grid resolution, and the mean ionisation fraction. However, the majority of these islands are very small overionised regions, typically consisting of 10 pixels or less, even though they contribute very little to the global ionisation fraction (approximately 1%). To speed up the bubble overlap step while sacrificing some small-scale precision, we introduce a free parameter called $N_{\text{cell,th}}$, which represents the "threshold cell number." This parameter enables the user to simultaneously treat all the ionised islands with fewer than $N_{\text{cell,th}}$ pixels when spreading the excess ionisation fraction they contain.

To illustrate this process, consider a x_{HII} field on a grid, with 100 separate and unconnected ionised islands that contain overlaps or overionised cells. If $N_{\text{cell,th}} = 0$, the algorithm distributes the excess ionisation fraction to neighbouring cells for each island individually. However, if $N_{\text{cell,th}} = 10$, all islands with less than 10 pixels are treated together. This means that the sum of the excess ionisation fraction in these islands is spread evenly over their combined borders.

To speed up the code, one can increase the value of $N_{\text{cell,th}}$, but at the cost of precision. However, for values of $N_{\text{cell,th}}$ up to a certain threshold, the impact on the 21-cm signal at the relevant scales ($0.1 < k < 1 \text{ Mpc}^{-1}$) remains negligible. To evaluate this effect, we generate an x_{HII} field on a 256^3 grid with a length of 147 cMpc and a halo catalogue containing 7.5 million halos, at redshift $z = 7$, from our Pkdgrav3 simulation. The field has a mean ionisation fraction $\bar{x}_{\text{HII}} = 0.5$. We repeat the bubble overlap procedure with varying values of $N_{\text{cell,th}}$ and compare the power spectra of the x_{HII} fields after redistributing the overionised cells. The results are shown in Fig. A1, where we plot the ratio between the x_{HII} power spectra for different values of $N_{\text{cell,th}}$ and the fiducial value ($N_{\text{cell,th}} = 0$).

After painting the ionised bubbles, we obtain 43,132 ionised isolated islands (or connected regions). The procedure takes 52 minutes

in total to go through each overionised region individually and spread the excess ionisation fraction. However, we can group together all the islands with less than 10, 40, 80, or 160 pixels to speed up the process. This reduces the time required to respectively 6, 2, 1.42, and 1.18 minutes. As shown in Fig. A1, the error on the power spectrum remains negligible up to $N_{\text{cell,th}} = 40$ (less than 1%), and even for $N_{\text{cell,th}} = 160$, it is less than 3% between $0.1 < k < 1 \text{ Mpc}^{-1}$.

In summary, the parameter $N_{\text{cell,th}}$ can be adjusted according to the required precision. Note that it scales with the total number of pixels on the grid.

APPENDIX B: CONVERGENCE TEST

We carry out a convergence check by varying the number of halo mass bins N_{bin} used to compute the profiles and the number of grid pixels N_{cell} when running BEoRN. We perform this comparison for a model similar to the *cutoff* model of Section 4 (the exact parametrization is not relevant for the purpose of this convergence test). Initially, we vary the number of mass bins N_{bin} . Our halo mass range spans 6.5 orders of magnitude in mass. We run BEoRN with 40, 80 and 120 bins in total on a grid with 256^3 pixels and present the resulting power spectra as dotted, dashed and solid lines in the left panel of Fig. B1. $N_{\text{bin}} = 80$ provides well-converged curves over the scales of interest at every redshift. Since the mass range depends on the resolution of the halo catalogues and is left free to the user, the relevant quantity to specify here is the number of mass bins per order of magnitude in halo mass. 80 bins spanning 6.5 orders of magnitude in mass is roughly equivalent to 12 bins per dex. Consequently, the user can select the minimum and maximum halo mass according to its halo catalogue and establish the number of mass bins required to achieve converged results.

Subsequently, we vary the number of pixels N_{cell} and present our results in the right panel of Fig. B1 for $N_{\text{cell}} = 128^3, 256^3, 512^3$ (corresponding to dotted, dashed and solid lines). The computing time scales with the number of pixels due to the FFT convolution to put profiles on the grid. $N_{\text{cell}} = 256^3$ yields relatively well-converged results. However, if a sub-percent precision is necessary, a higher number of mass bins and finer grid resolution may be preferable.

APPENDIX C: THE MEAN FREE PATH OF IONISING PHOTON IN EXCURSION-SET METHODS

To model the presence of unresolved dense small-scale absorbers inside ionised regions, semi-numerical excursion-set (ES) methods have introduced the parameter R_{max} (Furlanetto & Oh 2005; Zahn et al. 2011; Alvarez & Abel 2012). R_{max} is meant to characterise the mean free path (MFP) of ionising photons inside ionised regions. It sets the value of the maximum scale over which the density and ionising photon fields are smoothed during the excursion-set procedure. In other words, a photon emitted by a source of ionising radiation cannot contribute to ionising a point that is at a distance larger than R_{max} from the source centre.

In BEoRN, the mean free path of ionising photons is not a parameter. Instead, distances travelled by ionising photons are smoothly distributed. This means that in regions with clustered sources surrounded by large ionised bubbles, ionising photons can naturally travel larger distances (via the redistribution of overionised cells) than around isolated sources surrounded by neutral gas. The only parameter in BEoRN that could have a similar effect to R_{max} is the clumping factor C (see Eq. 16). However, it is unclear if there exists

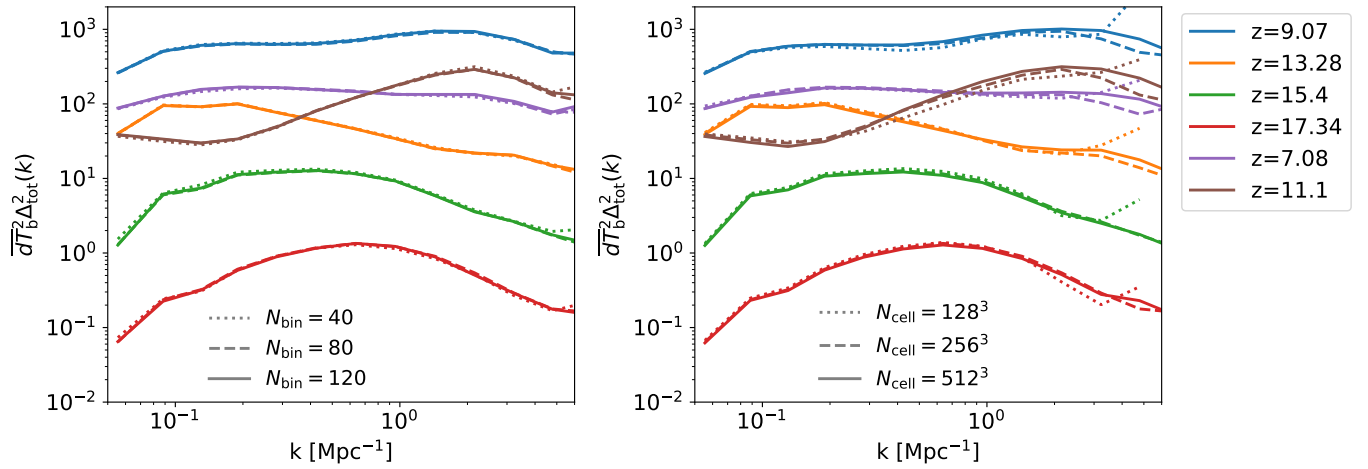


Figure B1. Halo mass and spatial resolution convergence check for BEoRN. The underlying astrophysical model is similar to the *cutoff* model from Sec. 4. *Left panel:* 21-cm dimensionless power spectra at various redshifts, varying the total number of halo mass bins N_{bin} . *Right panel:* Same as the left panel, but varying the total number of grid pixels N_{cell} .

a mapping between R_{max} and C , or even if the effect of R_{max} can be reproduced by varying C . Therefore, there is a fundamental difference in modelling between BEoRN and ES methods that rely on R_{max} .

To improve the accuracy of modelling the gradual absorption of ionising photons within ionised regions, Davies & Furlanetto (2022) proposed a new method that accounts for the smooth exponential attenuation of the ionising flux, resulting in a scale-dependent ionisation threshold or filter. This method differs from traditional ES methods that use a sharp maximum scale (R_{max}) for smoothing the density and ionising photon fields. The power spectrum predictions of the two methods differ, as we observed in our comparison of 21cmFAST and BEoRN.

To compare BEoRN to Davies & Furlanetto (2022), we use their MFP- $\epsilon(r)$ approach, which is relevant when sources of ionising photons are spatially resolved, as in BEoRN. We run BEoRN on top of our Pkdgrav3 halo catalogue using the same model as Davies & Furlanetto (2022) with a constant ionising efficiency and a minimum star-forming halo of $10^9 M_{\odot}$. We tune the number of ionising photons to achieve the same ionisation fractions as Davies & Furlanetto (2022) at redshifts $z = 7.5, 7, 6.5$ with mean ionisation fraction $x_{\text{HII}} = 0.2, 0.5, 0.8$. We then compare the resulting dimensionless power spectra of the x_{HII} fields $\Delta_{x_{\text{HII}}}^2$ and plot them in Fig. C1. The thick and dashed lines in the figure are taken from Davies & Furlanetto (2022), while the thin line is from BEoRN.

The smooth MFP implementation leads to a shift of power from large to small scales, which is in good agreement with BEoRN and is a significant improvement over traditional ES predictions. The match between BEoRN and Davies & Furlanetto (2022) is better, despite relying on different simulations and halo catalogues, with a maximum deviation of approximately 30%.

APPENDIX D: HALO MASS FUNCTION FROM OUR SIMULATION

The halo catalogues in our simulations, which consist of 2048^3 particles, were produced using the on-the-fly friend-of-friend algorithm in Pkdgrav3. We used a linking length of 0.2 times the initial mean interparticle distance and included only haloes with at least 10 DM

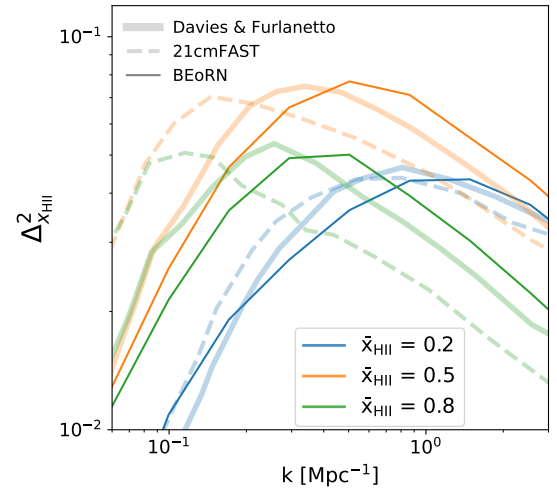


Figure C1. *Upper panel:* dimensionless power spectrum $\Delta_{x_{\text{HII}}}$ of the ionisation fraction field, as a function of Fourier mode k [Mpc^{-1}]. We compare the prediction from BEoRN (thin solid lines) with Davies & Furlanetto (2022) (solid thick lines) and the standard approach in 21cmFAST (dashed lines). The latter data is taken from fig. 7 of Davies & Furlanetto (2022). The three colours (blue, orange and green) correspond to different redshifts, $z = 7.5, 7, 6.5$, with mean ionisation fractions, $x_{\text{HII}} = 0.2, 0.5, 0.8$ respectively.

particles. To ensure transparency, we present the binned Halo Mass Function (HMF) from our catalogue, along with Poisson error bars, at various redshifts between $z \sim 21$ and $z \sim 6$, in Fig. D1. We also show our best-fit analytical mass function obtained through the extended Press-Schechter formalism (Press & Schechter 1974; Bond et al. 1991; Sheth et al. 2001). Our Sheth-Tormen mass function with a sharp-k filter provides a good fit to the HMF over the entire range of redshifts. The solid lines in Fig. D1 correspond to the Sheth-Tormen mass function using the following sharp-k HMF parameters: $c = 2.7$, $p = 0.3$, $q = 1$, $\delta_c = 1.675$, and $A = 0.322$ (see Schaeffer & Schneider 2021 for parameter definitions). Note that the analytical curve slightly underestimates the halo abundance at the lowest redshifts and overestimates it at the highest redshift. Tuning the value of the parameter c could improve the fit at a single redshift.

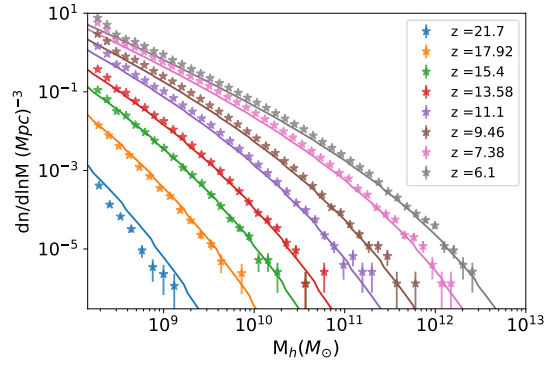


Figure D1. Halo mass function from our Pkdgrav3 N-body run (see section 4.1 for details on the simulation) with 2048^3 particles, and box size 147cMpc, at various redshifts. Solid lines correspond to a Sheth-Tormen mass function using a sharp-k filter (see Appendix. D for the parameter values). Error bars correspond to Poisson errors in each bin.